

MIGRATION AND GROWTH OF PROTOPLANETARY EMBRYOS III: MASS AND METALLICITY  
DEPENDENCE FOR FGKM MAIN-SEQUENCE STARSBEIBEI LIU<sup>1,2\*</sup>, XIAOJIA ZHANG<sup>3</sup>, DOUGLAS N. C. LIN<sup>2, 3, 4, 5</sup>  
*Submitted to the Astrophysical Journal*

## ABSTRACT

Radial velocity and transit surveys have found that the fraction of FGKM stars with close-in super-Earth(s) ( $\eta_{\oplus}$ ) is around 30%–50%, independent of the stellar mass  $M_*$  and metallicity  $Z_*$ . In contrast, the fraction of solar-type stars harboring one or more gas giants ( $\eta_J$ ) with masses  $M_p > 100 M_{\oplus}$  is nearly 10% – 15%, and it appears to increase with both  $M_*$  and  $Z_*$ . Regardless of the properties of their host stars, the total mass of some multiple super-Earth systems exceeds the core mass of Jupiter and Saturn. We suggest that both super-Earths and supercritical cores of gas giants were assembled from a population of embryos that underwent convergent type I migration from their birthplaces to a transition location between viscously heated and irradiation heated disk regions. We attribute the cause for the  $\eta_{\oplus}$ – $\eta_J$  dichotomy to conditions required for embryos to merge and to acquire supercritical core mass ( $M_c \sim 10 M_{\oplus}$ ) for the onset of efficient gaseous envelope accretion. We translate this condition into a critical disk accretion rate, and our analysis and simulation results show that it weakly depends on  $M_*$  and decreases with metallicity of disk gas  $Z_d$ . We find that embryos are more likely to merge into supercritical cores around relatively massive and metal-rich stars. This dependence accounts for the observed  $\eta_J$ – $M_*$ . We also consider the  $Z_d$ – $Z_*$  dispersed relationship and reproduce the observed  $\eta_J$ – $Z_*$  correlation.

*Subject headings:* methods: numerical – planetary systems – planet-disk interactions

## 1. INTRODUCTION

The rapidly accumulating data on exoplanets' mass ( $M_p$ ), radius ( $R_p$ ), semimajor axis ( $a$ ), period ( $P$ ), multiplicity, and their host stars' mass ( $M_*$ ) and metallicity ( $Z_*$ ) (Winn & Fabrycky 2015) provide valuable clues and meaningful constraints on the theory of planet formation. The widely adopted sequential accretion scenario is based on the assumption that the formation of gas giants is preceded by the assemblage of cores with masses in excess of a critical value ( $M_c \simeq 10 M_{\oplus}$ ) (Pollack et al. 1996). The building-blocks of these cores are evolved from protoplanetary embryos with dynamical isolation masses (Ida & Lin 2004a). The observed kinematic and structural diversity of exoplanets has provided solid evidence to support a major paradigm shift from the traditional *in situ* formation hypothesis based on the minimum mass nebula model (Hayashi 1981) to the concept that the proto-gas-giant planets' cores and super-Earth progenitors may have migrated extensively in their natal disks.

During their formation and growth, these embryos and cores tidally interact with their natal disks (Goldreich & Tremaine 1980; Kley & Nelson 2012; Baruteau et al. 2014). With masses up to a few  $M_{\oplus}$ , embedded embryos and cores do not exert sufficiently strong perturbations

to modify the disk structure (Lin & Papaloizou 1993). Nevertheless, the disk torque induces them to undergo type I migration (Ward 1997). Massive proto-gas giants do open gaps in the vicinity of their orbits, and they undergo type II migration (Lin & Papaloizou 1986). Models based on these effects have been invoked to account for the origin of hot Jupiters (Lin et al. 1996), resonant gas giants (Lee & Peale 2002), and super-Earths (Papaloizou & Szuszkiewicz 2005).

Early linear torque analysis (Tanaka et al. 2002) indicates that planets with  $M_p \simeq M_c$  and  $a = 1$  AU in disks with gas surface density ( $\Sigma_g$ ) and temperature ( $T_g$ ) comparable to those of the minimum mass solar nebula (MMSN) (Hayashi 1981), undergo inward type I migration on a time scale  $\tau_a (= a/\dot{a})$  of  $\lesssim 0.1$  Myr. This time scale is smaller than the time scales of disk depletion ( $\tau_{\text{dep}}$ ) and cores' growth through gas accretion ( $\tau_{c,\text{acc}}$ ). This issue has the embarrassment that type I migration may lead to a substantial loss of cores before they evolve into gas giants (Ida & Lin 2008).

In order to suppress the migration speed and solve this time scale challenge for the sequential accretion scenario, two approaches have been investigated. Masset et al. (2006) proposed that planets may be trapped near disk radii where the surface density  $\Sigma_g$  and temperature  $T_g$  undergo a transition. Such a transition may occur near the inner disk edge (Terquem 2003), boundary between dead and active zones (Hasegawa & Pudritz 2010), the outer edge of the gap opened by giant planets (Pierens & Nelson 2008) or the snow-line region (Cuzzi & Zahnle 2004). Near these transitional locations, planets' net tidal interaction with the disks may be suppressed. Alternatively, turbulent fluctuations in MHD disks produce additional stochastic torques, and the survival of the planets can be statistically determined by this tur-

<sup>1</sup> Anton Pannekoek institute for Astronomy, University of Amsterdam, the Netherlands

<sup>2</sup> Kavli Institute for Astronomy & Astrophysics, Peking University, Beijing, 100871, China

\* E-mail: bbliu1208@gmail.com

<sup>3</sup> Department of Astronomy and Astrophysics, University of California, Santa Cruz, CA 95064, USA

<sup>4</sup> Institute for Advanced Studies, Tsinghua University, Beijing, 100086, China

<sup>5</sup> National Astronomical Observatory of China, Beijing, 100012, China

bulent amplitude (Laughlin et al. 2004b; Nelson 2005).

Based on a series of numerical simulations for non-isothermal disks, Paardekooper et al. (2010, 2011) (hereafter PBK10, PBK11) systematically analyzed the tidal interaction between isolated embryos and disks with continuous  $\Sigma_g$  and  $T_g$  distributions. They showed that (1) embryos' migration rate and direction are determined by the sum of differential Lindblad ( $\Gamma_L$ ) and corotation ( $\Gamma_c$ ) torque, (2)  $\Gamma_L$  generally leads to orbital decay, (3) for some  $\Sigma_g$  and  $T_g$  distributions (characterized by their logarithmic gradient  $s \equiv \partial \ln \Sigma_g / \partial \ln r$  and  $\beta \equiv \partial \ln T_g / \partial \ln r$ ),  $\Gamma_c$  may induce a positive angular momentum transfer to the embryos, and (4) the strength of  $\Gamma_c$  may be saturated unless the unperturbed values of  $s$  and  $\beta$  can be retained in the corotation region by the combined effects of viscous and thermal diffusion. Several authors (Lyra et al. 2010; Bitsch et al. 2013; Baillié et al. 2015) have suggested that embryos may migrate to and accumulate near some trapping radius ( $r_{\text{trap}}$ ) where  $\Sigma_g$  and  $T_g$  distributions undergo such transitions.

PBK10, 11 summarized their numerical results into a set of a very useful analytic approximations for the torque formula. Several investigators have applied this prescription to various disk models and constructed modified N-body schemes to simulate the outcome of embryos migration. Pierens et al. (2013) showed that multiple embryos may converge into resonant convoys and these merger barriers may be bypassed by a large number of embryos or stochastic force due to disk turbulence. Cossou et al. (2014) proposed that  $r_{\text{trap}}$  is located near the opacity transition region, where the disk temperature gradient is steep. They showed that convergent embryos may merge during the early phase of disk evolution. Coleman & Nelson (2014) used a different disk model to simulate both the formation and migration of super-Earths and gas giants. They found that unless gas giants were formed at large radii during the advanced stages of disk evolution, a large fraction of them would migrate to the proximity of their host stars.

In this series papers (Zhang et al. 2014; Liu et al. 2015, hereafter Papers I and II respectively), we also constructed a Hermite-Embryo code, based on the application of PBK10's torque formula to a self-consistent disk model (Garaud & Lin 2007, hereafter GL07). With this approach, we systematically determine the condition for core formation around solar-type G stars. We show the following (1) In the viscously heated inner disk, the corotation torque leads to a net transfer of angular momentum from the protostellar disks to the embryo, whereas the direction of angular momentum transport is reversed in the irradiated outer region. (2) The corotation torque is saturated (weakened) for embryos with  $M_p$  outside a factor of  $(2h)^{-2/3}$  ( $h$  is the aspect ratio of the disk) from an optimum value ( $M_{\text{opt}}$ ); thus, embryos with  $(2h)^{2/3} M_{\text{opt}} < M_p < (2h)^{-2/3} M_{\text{opt}}$  undergo convergent migration toward a transition radius ( $r_{\text{trans}}$ ) separating these regions (Kretke & Lin 2012). The magnitudes of  $M_{\text{opt}}$  and  $r_{\text{trans}}$  are  $4 M_{\oplus}$  and 1.4 AU in disks with  $\dot{M}_g = 10^{-8} M_{\odot} \text{ yr}^{-1}$ ;  $11 M_{\oplus}$  and 7.1 AU for  $\dot{M}_g = 10^{-7} M_{\odot} \text{ yr}^{-1}$ . (3) We also demonstrated that in disks with  $\dot{M}_g \lesssim 10^{-8} M_{\odot} \text{ yr}^{-1}$ , embryos converge relatively slowly and they capture each other into

their mutual mean motion resonances (MMRs). Thereafter, they migrate together as a convoy of embryos with  $M_p < M_c$  and are trapped at  $r_{\text{trap}} = r_{\text{trans}}$ . (4) However, in disks with  $\dot{M}_g \sim 10^{-7} M_{\odot} \text{ yr}^{-1}$ , migrating embryos converge rapidly toward  $r_{\text{trans}}$ , bypass the MMR barrier, and cross each other's orbits. (5) After many close encounters, embryos collide and merge into large cores, retain outside and evolve into gas giants. These results are qualitatively in agreement with previous contributions by others. We provided the quantitative criteria to indicate that the ubiquitous presence of super-Earths and the limited frequency of gas giants around solar-type stars are the manifestation of a threshold condition for core formation that depends on the magnitude of the disk accretion rate ( $\dot{M}_g$ ).

In this paper, we generalize these results to determine the dependence of  $\eta_J$  and  $\eta_{\oplus}$  around stars with different  $M_*$  and  $Z_*$ . Some basic formulae used here are already presented in Paper II. In §2, we first obtain observational clues from multiple transiting planet systems in the latest Kepler database. We highlight that  $\eta_{\oplus}$  appears to be independent of  $M_*$  and  $Z_*$ , but  $\eta_J$  generally increases with  $M_*$  and  $Z_*$ . In order to account for these observational properties with our threshold core-formation scenario, we briefly recapitulate the dependence of  $M_{\text{opt}}$  and  $r_{\text{trans}}$  on  $\dot{M}_g$ . Based on the observational data, we introduce an approximate prescription for  $\dot{M}_g$ 's dependence on  $M_*$  and  $Z_*$ . With much more limited observational constraints, we assume that (1) The metallicity of the disk gas  $Z_d$  increases with  $Z_*$  with a dispersion ( $\Delta_Z$ ) and (2)  $\dot{M}_g$  is independent of  $Z_*$ . The isolation mass of embryos ( $M_{\text{iso}}$ ) is determined by the surface density of heavy elements ( $\Sigma_d \propto 10^{-Z_d}$ ). We show that the magnitudes of  $\tau_a$ ,  $r_{\text{trans}}$ , viscosity, and  $M_{\text{opt}}$  are also functions of  $Z_d$  through the opacity dependence in the disk structure.

We recapitulate the necessary disk condition for the formation of critical-mass cores in §3. We generalize the prescription and analytic approximations in Paper II to a range of  $M_*$  and  $Z_d$ . We present several simulation models for embryos' migration around different stellar masses in §4. These results are generated with the Hermite-Embryo code. We show that regardless of  $Z_d$ , a population of super-Earths may accumulate near  $r_{\text{trans}}$ . But they would not be able to bypass the MMR barrier and merge into cores unless the gas accretion rate ( $\dot{M}_g$ ) in their natal disks exceeds some critical value ( $\dot{M}_{\text{res}}$ ). Based on the observed  $\dot{M}_g$  dependence on  $M_*$ , we find (1) only a small fraction of solar-type stars ( $\eta_{\dot{M}}$ ) satisfy this core-formation criterion and (2)  $\eta_{\dot{M}}$  increases with  $M_*$ . Under the assumption that  $\eta_{\dot{M}}$  corresponds to  $\eta_J$ , we reproduce the observed  $\eta_J$ - $M_*$  correlation among FGKM main-sequence stars.

In §5, we focus on the  $\eta_J$ - $Z_*$  correlation around solar-type stars. We show that although  $M_{\text{iso}}$  and  $r_{\text{trans}}$  are increasing functions of  $Z_d$ , the formation probability of cores does not depend sensitively on the initial total mass of embryos. However, in a layer accretion disk model, the effective viscosity  $\nu$  may decrease and  $\Sigma_g$  increase with  $Z_d$  such that migrating embryos are likely to bypass the MMR barrier and converge near  $r_{\text{trans}}$  in metal-rich disks. The close packing of embryos enhances their

merger probability and promotes the emergence of cores and gas giants. We reproduce the observed  $\eta_J - Z_*$  correlation by taking into account the correlation and dispersion between  $Z_d$  and  $Z_*$ . Finally, in §6, we summarize our results and discuss their implications.

## 2. OBSERVATIONAL PROPERTIES

### 2.1. Frequency of planets in different stellar environment

Radial velocity (RV) and transit surveys indicate that while nearly 10% – 15% of solar-type stars harbor one or more gas giant planets (Marcy et al. 2008; Cumming et al. 2008), they are rarely found around late dwarfs (Endl et al. 2006; Bonfils et al. 2013). This fraction ( $\eta_J$ ) appears to increase with  $M_*$  among subgiant and giant stars more massive than the Sun (Johnson et al. 2007, 2010; Jones et al. 2016). However, the fraction of stars that contain super-Earths ( $\eta_\oplus$ ) is almost 30% – 50% and appears to be at least as abundant in M stars as in FGK stars (Bonfils et al. 2013; Howard et al. 2012; Fressin et al. 2013; Dressing & Charbonneau 2013; Mulders et al. 2015). Here super-Earths categorically refer to the low-mass ( $M_p < 30 M_\oplus$ ) and modest-size ( $R_p < 4 R_\oplus$ ) planets with period  $P < 100$  days, in contrast to the more massive gas giants with period up to a few years. The magnitude of  $\eta_J$  is also an increasing function of  $Z_*$  (Santos et al. 2004; Fischer & Valenti 2005; Sousa et al. 2011; Mortier et al. 2013), whereas  $\eta_\oplus$  appears to be independent of  $Z_*$  (Sousa et al. 2008; Schlaufman & Laughlin 2011; Buchhave et al. 2012; Wang & Fischer 2015; Buchhave et al. 2014; Schlaufman 2015). Combined the RV measurement and transit light curve, some inferred super-Earths appear to have substantial gaseous atmospheres. In contrast to the formation history of terrestrial planets in our solar system, these super-Earths may have acquired most of their masses prior to the depletion of the disk gas (Lopez & Fortney 2014).

There have been several attempts to account for both the  $\eta_J - M_*$  and  $\eta_J - Z_*$  correlations (Laughlin et al. 2004a; Ida & Lin 2004b, 2005; Mordasini et al. 2012). These models generally assume that the total mass of building-block planetesimals and embryos in the disk is a fixed fraction of the heavy elements in the central stars.

In Paper II, we proposed an alternative minimum planetary building-block scenario based on the confirmed planets in the multiple-planet systems. Kepler data showed that even though a large number of individual super-Earths have mass ( $M_p$ ) smaller than the critical mass ( $M_c$ ), the total mass  $M_s$  in most multi-planetary systems around individual host stars exceeds  $M_c$  (Figure 1 in Paper II). The common existence of such multiple super-Earth systems suggests that there is no lack of heavy elements in their natal disks. Nevertheless, the lack of gas giants around most solar-type stars may be due to the inability of a sufficient fraction of all available building-block materials to be collected into a few supercritical cores with  $M_p \geq M_c$ .

In this paper, we consider the formation efficiency of cores around stars with different  $M_*$  and  $Z_*$ . We first analyze the implication of observational data. The ground-based observations are contaminated by heterogeneous observational selection effects. But the Kepler target stars provide a controlled sam-

ple with well-stated observational selection criteria (Dong & Zhu 2013). The latest Kepler data release (<http://exoplanetarchive.ipac.caltech.edu/index.html>) categorizes 4664 planetary candidates. Most of these transiting objects are potentially super-Earths with  $R_p \sim 1 - 4 R_\oplus$ . A fraction of them have been confirmed by follow-up RV or transit timing observations (Marcy et al. 2014).

In order to infer  $M_p$  from the Kepler data, we adopted an empirical  $M_p - R_p$  relationship extrapolated from solar system planets in Paper II (Lissauer et al. 2011) that

$$M_p \simeq M_1 (R_p / R_\oplus)^{\eta_M}, \quad (1)$$

where  $\eta_M = 2.06$  and the normalized mass  $M_1 = 1 M_\oplus$ . Based on the follow-up RV determination, Dressing et al. (2015) find that the solar system extrapolation from Zeng & Sasselov (2013) matches well with the  $M_p - R_p$  correlation among super-Earths with  $R_p < 1.6 R_\oplus$ . The latest two-layer metal/rock planet model (Zeng et al. 2016) suggests  $\eta_M = 3.7$ ,  $M_1 = (1.07 - 0.21 \times \text{cmf})^{0.27}$  for planets with  $R_p < 1.75 R_\oplus$ , where cmf refers to a core mass fraction between 0 and 0.4. There is a large dispersion among more massive super-Earths. Wu & Lithwick (2013) used measured mass from transit timing variations (TTVs) to get  $\eta_M = 1$  and  $M_1 = 3 M_\oplus$ . Weiss & Marcy (2014) fitted both RV and TTV data with similar  $\eta_M = 0.93$  and  $M_1 = 2.69 M_\oplus$  for  $1.5 R_\oplus < R_p < 4 R_\oplus$ .

Combining the data obtained from both RV and TTV methods, Rogers (2015) and Wolfgang et al. (2015) found that  $M_p$  generally increases with  $R_p$  but with a wide dispersion. Quantitatively, for each observationally measured  $R_p$ , the inferred  $M'_p$  may have a Gaussian distribution,

$$\frac{dN(M'_p, R_p)}{dM'_p} = \frac{N}{M_\oplus} \exp \left[ -\frac{[\log M'_p(R_p) - \log M_p(R_p)]^2}{\Delta_{M_p}} \right] \quad (2)$$

where  $\Delta_{M_p} \simeq 0.3$  is a factor of 2 mass dispersion in logarithm. Instead of a piecewise function, we choose observed masses and radii relation with a single power law plus extra intrinsic scatter shown above where  $\eta_M = 1.8$  and  $M_1 = 1.6 M_\oplus$  for planets with  $R_p < 8 R_\oplus$  (Wolfgang et al. 2015).

We plot the individual  $M_p$  for the 2007 confirmed/candidate planets from the dataset as a function of their host stellar mass. We obtain  $M_*$  from the Huber et al. (2014)'s stellar catalog and the Dartmouth Stellar Evolution Program (DSEP). We adopt the values of  $\eta_M$  and  $M_1$  for two deterministic prescriptions from equation (1) (Figure 1) and one probabilistic  $M_p - R_p$  prescription from equation (2) (Figure 2 and 3). Comparison of the results obtained with different  $M_p - R_p$  prescriptions shows no noticeable differences in the inferred  $M_p$  and  $M_s$  distribution around stars with different  $M_*$  and  $Z_*$  values.

Based on the statistical prescription of equation (2), we plot in Figure 2, the individual planetary mass ( $M_p$ ) and the total (detected) planetary mass ( $M_s$ ) distribution for the 820 confirmed/candidate multiple-planet systems. Using the same approach, we also plot in Figure 3 the  $M_p$  distribution for the 421 confirmed/candidate planets and the total mass  $M_s$  distribution for the 159 multiple-planet systems around metal-rich and metal-

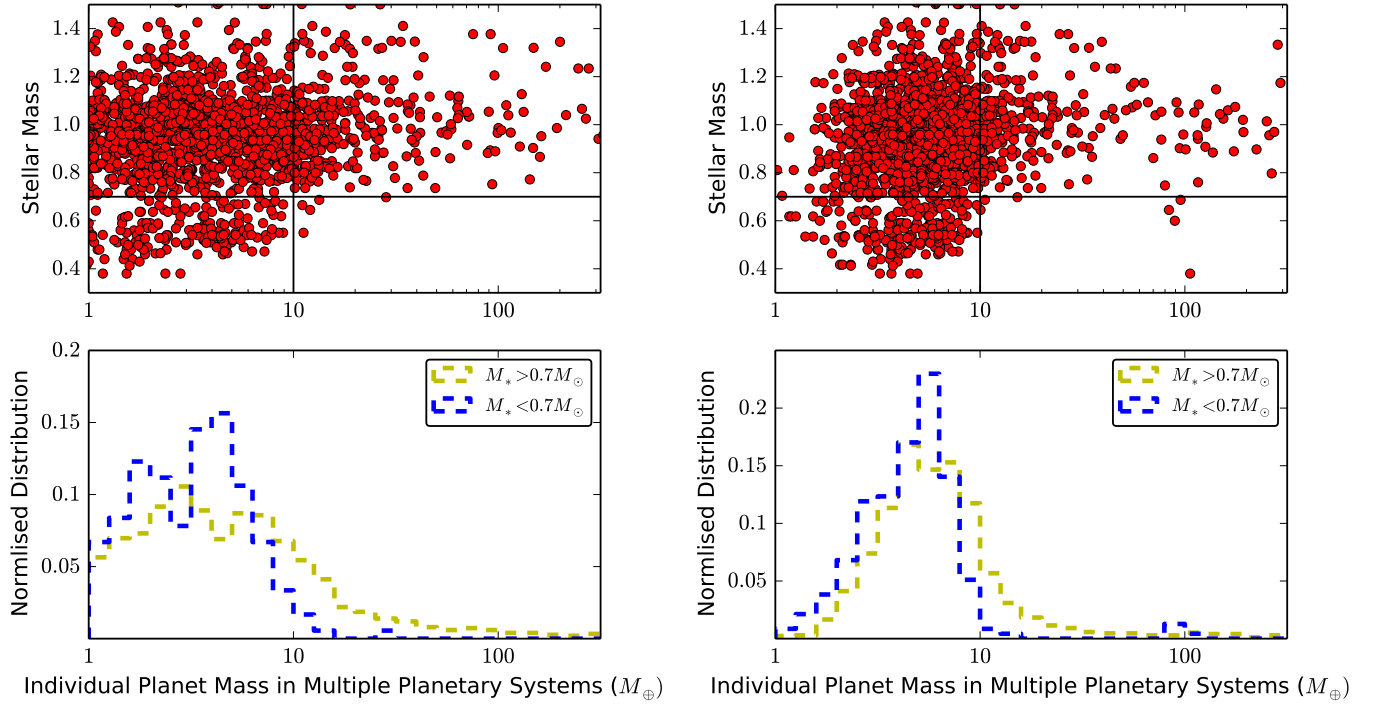


FIG. 1.— single planet mass  $M_p$  (red dots) versus the mass of their host stars ( $M_*$ ). The horizontal black line indicates the critical stellar mass ( $M_*$ ) and vertical black line marks the critical planet mass  $M_c$  for efficient gas accretion. The left panel adopts  $\eta_M = 2.06$  and  $M_1 = 1$  and the right panel uses  $\eta_M = 1$  and  $M_1 = 3$ . The planets' data are obtained from the Kepler's database in NASA Exoplanet Archive, and the stellar parameters are adopted from the Huber et al. (2014) catalog.

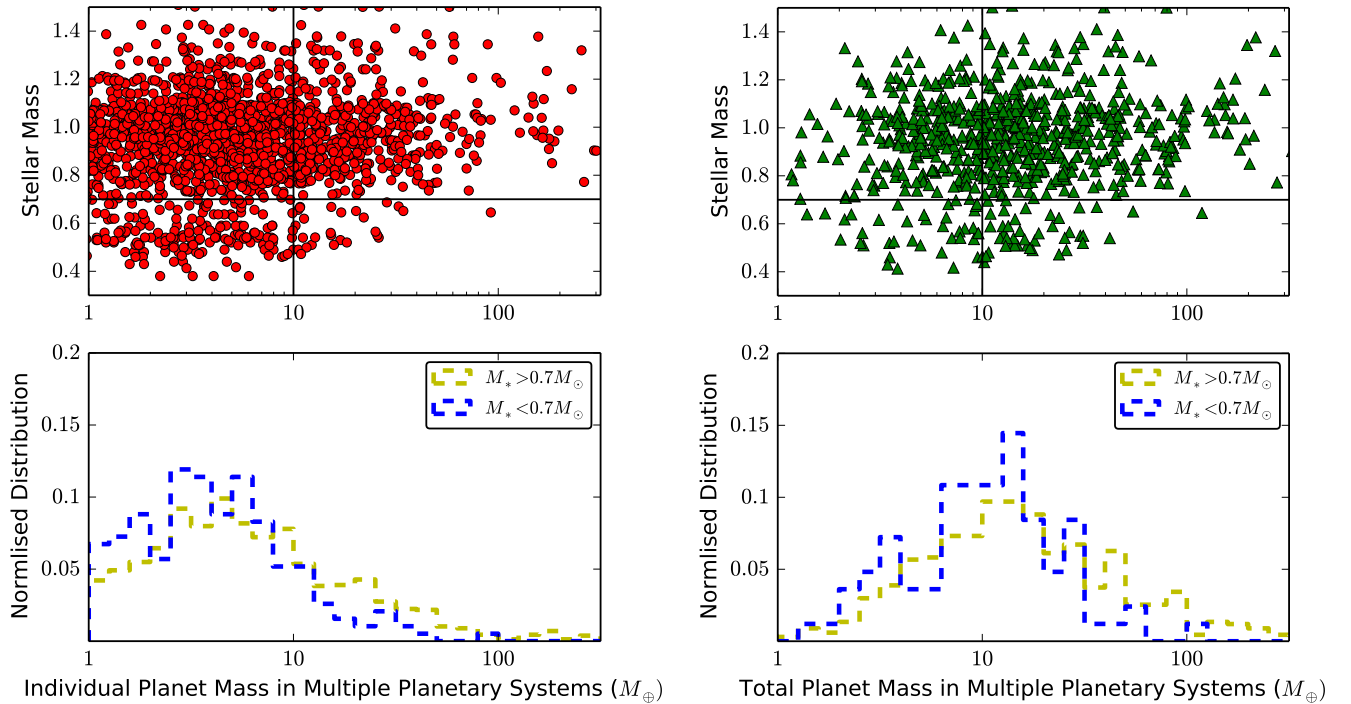


FIG. 2.— Top panels: single planet mass  $M_p$  (red dots in left panel) and total (detected) planet mass  $M_s$  in individual systems (green triangles in right panel) versus the mass of their host stars ( $M_*$ ). The values of  $M_p$  and  $M_s$  are obtained from the statistical prescription in Eq 2. The horizontal black line indicates the critical stellar mass ( $M_*$ ) and the vertical black line separates the critical planet mass ( $M_c = 10 M_\oplus$ ) for efficient gas accretion. Bottom panels: normalized distribution of  $M_p$  (left) and  $M_s$  (right) as functions of  $M_*$ . The yellow dashed histogram represents the samples with  $M_* > 0.7 M_\odot$ , while the blue dashed histogram represents samples with  $M_* < 0.7 M_\odot$ . All the planets' data are obtained from the Kepler's database in NASA Exoplanet Archive, and the stellar information is from the Huber et al. (2014)'s catalog.

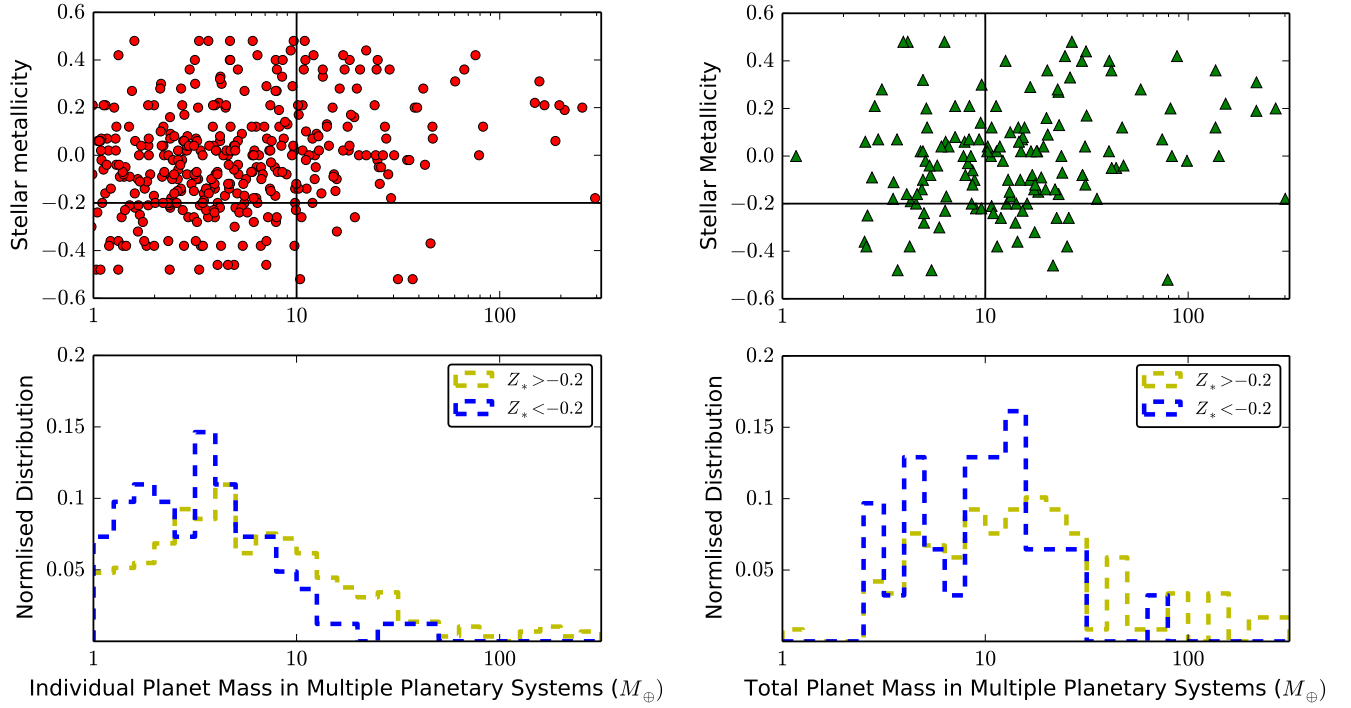


FIG. 3.— Top panels: single planet mass  $M_p$  (red dots on the left) and  $M_s$  (green triangles on the right) versus their host stars' metallicity ( $Z_*$ ). The values of  $M_p$  and  $M_s$  are obtained from the statistical prescription in Eq 2. The horizontal black line indicates  $Z_* = -0.2$  which appears to be the threshold metallicity for stars with gas giant planets, and the vertical black line corresponds to  $M_p = M_c (= 10 M_\oplus)$ , which is the conventional condition for efficient gas accretion. Bottom panels: normalized distribution  $M_p$  (left) and  $M_s$  (right) distributions. The yellow dashed histograms represent the samples with  $Z_* > -0.2$ , while the blue dashed histogram represents samples with  $Z_* < -0.2$ . The planets' data are obtained from the Kepler's database in NASA Exoplanet Archive, and the stellar parameters are adopted from the Huber et al. (2014) catalog. Only the SPE samples (with sufficiently accurate spectroscopic  $Z_*$ ) are included in this figure.

deficient stars respectively. The number of data entries in Figure 3 is smaller than that in Figure 2 because it includes only the high-resolution spectroscopy “SPE” sample, which excludes host stars with average metallicity error bars larger than 0.15 dex.

In Figures 2 and 3, red dots and green triangles represent the single planetary mass  $M_p$  and the total mass  $M_s$  of multiple-planet systems around individual host stars. The top panels of Figure 2 show  $M_p$  (left) and  $M_s$  (right) as a function of  $M_*$ . In Figure 2, black lines correspond to  $10 M_\oplus$  for the critical core mass and  $0.7 M_\odot$  for stellar mass of K and M main-sequence dwarfs. Bottom panels show the histogram of their normalized  $M_p$  (left) and  $M_s$  (right) distributions with host stars  $M_* > 0.7 M_\odot$  (yellow) and  $M_* < 0.7 M_\odot$  (blue).

The same symbols are used in Figure 3 for the  $M_p - Z_*$  and  $M_s - Z_*$  distribution. The horizontal black lines in the top panels present the critical value of  $Z_* = -0.2$ . Precise measurement of  $M_*$  and  $Z_*$  of all Kepler samples including some excluded planets may be significantly improved by follow-up observations with spectroscopic survey telescopes such as SDSS or LAMOST (private discussion with Yang Huang and Subo Dong).

Figures 2 and 3 show that very few individual planets have  $M_p$  in excess of the critical core mass ( $M_c \simeq 10 M_\oplus$ ) typically around late-type K and M dwarfs (with  $M_* < 0.7 M_\odot$ ) and metal-deficient stars (with  $Z_* < -0.2$ ). But the total mass of planets in multiple systems  $M_s$  is substantially larger than  $10 M_\oplus$  regardless of their host stars’  $M_*$  and  $Z_*$ . Around some metal-deficient and K and M dwarf stars,  $M_s$  can extend to  $30 - 40 M_\oplus$ . While the  $M_p$  distribution above  $M_c$  (left bottom panel of Figure 2 and 3) for relative massive and metal-rich stars differs intrinsically from those with smaller  $M_*$  and  $Z_*$ , the discrepancy of their total mass distribution is relatively small for all stars with  $M_s < 40 M_\oplus$ .

These figures pose challenges to the conventional planet formation scenarios based on the following assumptions: (1) a nearly constant fraction of the heavy elements in their host stars is retained to form protoplanetary building blocks, and (2) the formation probability of gas giants is determined by the total mass of protoplanetary embryos in their natal disks.

These figures also indicate that even around low-mass and metal-deficient stars, there is still an adequate supply of building-block materials to form a critical mass core and initiate runaway gas accretion if these low-mass super-Earths were able to merge with each other. How these low-mass super-Earths are organized and assembled together in protoplanetary disks is a more crucial issue that modulates the gas giant formation efficiency. Based on that consideration, we search for decisive factors that affect the efficiency of gas giant formation. In a straightforward approach we fix one condition (the total mass of embryos) and vary the other variables (i.e.,  $M_*$  and  $\dot{M}_g$  in section 4) in our simulations.

Another interesting issue is the critical condition for the onset of efficient gas accretion. The critical mass  $M_c$  is determined by the rate of heat transport from the core ( $R_c$ ) to the Roche radius ( $R_R$ ). This process is dominated by convection close to  $R_c$  and by radiative diffusion in the tenuous region near  $R_R$ . Since the radiative flux is inversely proportional to the opacity, the magnitude of

$M_c$  determined from 1D quasi-hydrostatic calculations increases with the local  $Z_d$  (Ikoma et al. 2000; Hubickyj et al. 2005; Movshovitz et al. 2010). The implication of these models is that around metal-deficient stars, a larger fraction of cores with  $M_p \sim 10 M_\oplus$  may evolve into gas giants rather than become super-Earths. The results in Figures 3 show that (1) the fraction of super-Earths with  $M_p \sim 5 - 10 M_\oplus$  remains modest and gas giants are extremely rare around metal-deficient stars, and (2) the drop-off of the normalized  $M_p$  distribution increases with  $Z_*$ . These features suggest that the transitional threshold from super-Earths to gas giants may be weakly but not principally determined by opacity of the accreted gas.

## 2.2. Link Type I torque with observational properties of protostellar disks

The common existence of super-Earths and rarity of gas giants, especially around low  $M_*$  and  $Z_*$  stars, suggests that it is inappropriate to simply attribute the observed  $\eta_J - M_*$  and  $\eta_J - Z_*$  correlation to a dependence on the availability of building-block material. Instead, we suggest that they may be due to the marginal conditions required for protoplanetary embryos to migrate, converge, cross each other’s orbit, and merge into proto-gas-giant cores in their natal disks. In this scenario, the condition for super-Earth embryos to evolve into super-critical cores is determined by the rate of their migration,  $\dot{a}$  (Paper II). Analytic derivation and numerical simulations (Goldreich & Tremaine 1980; Baruteau et al. 2014) show that several Earth-mass planet exerts a net torque

$$\Gamma = f_\Gamma(s, \beta, p_\nu, p_\xi) \Gamma_0 = f_\Gamma(s, \beta, p_\nu, p_\xi) (q/h)^2 \Sigma_p r_p^4 \Omega_p^2 \quad (3)$$

through their Lindblad and corotation resonances. In the above equation,  $q = M_p/M_*$ ,  $\Sigma_p$ ,  $h$ , and  $\Omega_p$  are the disk surface density, aspect ratio, and Keplerian frequency at the planet’s location  $r_p$ . The coefficient  $f_\Gamma$  is a function of  $s$ ,  $\beta$ , dimensionless parameters  $p_\nu = (2/3)(R_e x_s^3)^{1/2}$  and  $p_\xi = (R_e x_s^3/P_t)^{1/2}$  where  $R_e = \Omega_p r_p^2/\nu$  and  $P_t = \nu/\psi$  are the Reynolds and Prandtl numbers, respectively,  $\nu$  and  $\psi$  are the viscosity and radiative diffusion coefficients, and  $x_s \simeq (q/h)^{1/2}$  is the dimensionless width of the horseshoe region.

The total torque leads to a change in the planet’s semi-major axis at a rate

$$\dot{a} = \frac{2f_a(s, \beta, p_\nu, p_\xi) q \Sigma_p r_p^2}{h^2 M_*} r_p \Omega_p \quad (4)$$

where  $f_a(s, \beta, p_\nu, p_\xi) = \sum f_{\Gamma,i}(s, \beta, p_\nu, p_\xi)$  and the index  $i$  refers to components including the differential Lindblad and corotation torque. In the above expression, the migration rate is an increasing function of the disk surface density  $\Sigma_p$  at  $r_p$ .

Direct observational determination of disks’  $\Sigma_g$  and  $T_g$  is challenging since the inner region of the disk is optically thick. Although the disk becomes optically thin at relatively large radii, the bulk disk mass derived from (sub)millimeter dust observation still depends on poorly known dust opacity and gas-to-dust ratio. The uncertainties of CO measurement are due to the condensation of gas onto grains and photodissociation from external UV radiation by nearby OB stars. However, both the  $\Sigma_g$

and  $T_g$  distributions (i.e.  $s$  and  $\beta$ ) are expected to be correlated with  $\dot{M}_g$ . Based on the observed values of  $\dot{M}_g$  from disks around classical T Tauri and the well adopted  $\alpha$  prescription for viscosity (Shakura & Sunyaev 1973; Ruden & Lin 1986; Hartmann 1998), we find that the condition for the formation of supercritical-mass cores is marginally satisfied in protostellar disks around solar-type stars (Paper II).

### 2.3. Disk properties around different-mass host stars

Here we extend this embryo migration scenario for stars with different  $M_*$  and  $Z_*$  through the dependence of  $\Sigma_g$  and  $T_g$  distribution in their circumstellar disks. Statistical observational data of protostellar disks indicate that (1) the average accretion rate ( $\dot{M}_a$ ) is an increasing function of  $M_*$  with a dispersion ( $\Delta\dot{M}_g$ ), (2) the magnitude of  $\dot{M}_a$  decreases with time, and (3) there is no direct evidence that  $\dot{M}_a$  correlates with  $Z_*$  or  $Z_d$ .

Quantitative measurements (Hartmann et al. 1998; Natta et al. 2006; Manara et al. 2012; Ercolano et al. 2014; Da Rio et al. 2014) have been approximated by

$$\dot{M}_a = \dot{M}_{a\odot} m_*^{\eta_b} (t/\tau_{\text{dep}})^{-\eta_a} \quad (5)$$

where  $m_* = M_*/M_\odot$  and  $\dot{M}_{a\odot} \sim 5 \times 10^{-8} M_\odot \text{ yr}^{-1}$  corresponds to the average value of  $\dot{M}_g$  for solar-mass T Tauri stars. The time and mass dependences are fitted power-law functions with indices  $\eta_a \sim 1.0 - 1.4$  and  $\eta_b \sim 1.3 - 2.0$ .

For individual stars, we also introduce a Gaussian distribution function

$$\begin{aligned} dN/d\dot{M}_g &= A_0 \exp \left[ - \left( \frac{\log \dot{M}_g - \log \dot{M}_a}{\Delta \dot{M}_a} \right)^2 \right] \\ &= A_0 \exp \left[ - \left( \frac{\log(\dot{M}_g/\dot{M}_a)}{\Delta \dot{M}_a} \right)^2 \right] \end{aligned} \quad (6)$$

where  $\Delta \dot{M}_a = \log(\Delta \dot{M}_a/\dot{M}_a)$  and  $A_0$  is a normalized factor. Based on this expression, we can determine that the fraction of stars ( $\eta_{\dot{M}}$ ) with a given age and mass has  $\dot{M}_g$  larger than some fiducial value  $\dot{M}_f(M_*, Z_*)$  such that

$$\eta_{\dot{M}}(\dot{M}_f, M_*) = \frac{N(\dot{M}_g > \dot{M}_f)}{N_{\text{tot}}} = \frac{1}{2} \text{erfc} \left( \frac{\log \dot{M}_f/\dot{M}_a(M_*)}{\Delta \dot{M}_a} \right). \quad (7)$$

The expression of equation (5) is for stars with age comparable to or longer than the disk depletion time scale  $\tau_{\text{dep}} (\sim 3 - 5 \text{ Myr})$ . We are mostly interested in the active phase II of disk evolution around classical T Tauri stars when  $\dot{M}_a$  is relatively large. Within  $\sim \tau_{\text{dep}}/2$ , we can neglect the time dependence in  $\dot{M}_a$  so that equation (5) reduces to  $\dot{M}_a = \dot{M}_{a\odot} m_*^{\eta_b}$ . For illustration, we choose  $\dot{M}_{a\odot} = 5 \times 10^{-8} M_\odot \text{ yr}^{-1}$ ,  $\Delta \dot{M}_a = 1$  (from Figure 3 of Garcia Lopez et al. 2006), and  $\eta_b = 2$ . The  $\eta_{\dot{M}} - \dot{M}_g$  correlations are shown in the left panel of Figure 4 for three different  $M_*(= 0.5, 1, 2 M_\odot)$ .

In the next three sections, we determine the threshold disk accretion rate  $\dot{M}_f(M_*, Z_d)$  above which embryos

merge into retainable cores. For illustrative purposes, we introduce an  $\eta_{\dot{M}} - M_*$  correlation with an idealized power-law  $m_*$  dependence such that

$$\dot{M}_f(M_*) = \dot{M}_{cr}(M_\odot) m_*^{\eta_c} \quad (8)$$

where the normalization factor  $\dot{M}_{cr}(M_\odot) \sim 10^{-8} - 10^{-7} M_\odot \text{ yr}^{-1}$  for  $\alpha_\nu = 10^{-3}$  (Paper II). Although equation (8) takes into account the intrinsic dispersion in  $\dot{M}_g$  for different values of  $M_*$ , we have neglected the  $Z_d$  dependence due to the lack of any direct measurement of  $Z_d$  and  $\Sigma_d$ . It is customary to assume  $Z_d = Z_*$  because all of their contents were accreted onto the central stars through protostellar disks. In §5, we list some physical effects, which may introduce dispersions to the  $Z_d - Z_*$  correlation. This dispersion is incorporated with a general expression for  $\dot{M}_f(M_*, Z_d)$  (as  $\dot{m}_{g \text{ res}}$  in Eq. 30) in the evaluation of  $\eta_J(M_*, Z_*)$ .

In the right panel of Figure 4, we plot the  $\eta_{\dot{M}} - M_*$  diagram with different  $\eta_c$  (solid line for  $\eta_c = 0$  and dashed line for  $\eta_c = 1$ ). The red and blue colors correspond to  $\dot{M}_{c0} = 1 \times 10^{-7} M_\odot \text{ yr}^{-1}$  and  $5 \times 10^{-8} M_\odot \text{ yr}^{-1}$ , respectively. When considering the range of  $\dot{M}_{cr}$  for  $M_* = 1 M_\odot$ , we obtain an  $\eta_{\dot{M}}$  of  $\sim 0.3 - 0.5$ .

The quantity  $\eta_{\dot{M}}$  indicates the fraction of stars around which cores may form with  $M_p > M_c$ . Some of the cores may have  $M_p > M_{\text{opt}} + \Delta M$  such that their corotation torque would be saturated (weakened). Unless they can significantly modify the  $\Sigma_g$  distribution near their orbit (i.e., open up gaps), such massive cores would migrate toward and be consumed by their host stars. In this regard, the magnitude of  $\eta_{\dot{M}}$  should be considered as an upper limit for  $\eta_J$ .

## 3. MIGRATION AND GROWTH FROM EMBRYOS TO GAS GIANTS

In this section, we construct an analytic expression for the critical accretion rate  $\dot{M}_f(M_*, Z_*)$  above which embryos can bypass the MMR barriers and merge into cores. We normalize the disk parameters (see Paper II)  $\dot{m}_g \equiv \dot{M}_g/10^{-9} M_\odot \text{ yr}^{-1}$ ,  $m_* \equiv M_*/M_\odot$ ,  $l_* \equiv L_*/L_\odot$ ,  $r_{\text{AU}} \equiv r/\text{AU}$ ,  $\alpha_3 \equiv \alpha_\nu/10^{-3}$  where  $L_*$  and  $L_\odot$  are the stellar and solar luminosity, respectively, the opacity is  $\kappa = 0.02 \kappa_0 T_g$  representing grain abundance similar to that of protostellar disks,  $P = m_*^{-1/2} r_{\text{AU}}^{3/2} \text{ yr}$  is the orbital period,  $Z_d$  is the disk-metallicity enhancement factor relative to the Sun and  $\eta_{\text{ice}}$  (1 inside the ice line and 4 outside it) represents the enhancement factor for the condensed-ice contribution to the planetesimal building-block material.

### 3.1. Embryos' Isolation Mass and Type I Migration Timescale

With a feeding zone width of  $\sim 10 R_R$ , the embryos attain their isolation mass

$$M_{\text{iso}} \simeq 0.16 \left( \frac{\Sigma_d}{10 \text{ g cm}^{-2}} \right)^{3/2} m_*^{-1/2} r_{\text{AU}}^3 M_\oplus \quad (9)$$

on a growth time scale

$$\tau_{c, \text{acc}} \simeq \left( \frac{r}{R_p} \right) \left( \frac{M_p}{\Sigma_d r^2} \right) \left( \frac{M_p}{M_*} \right)^{-1/3} P \quad (10)$$



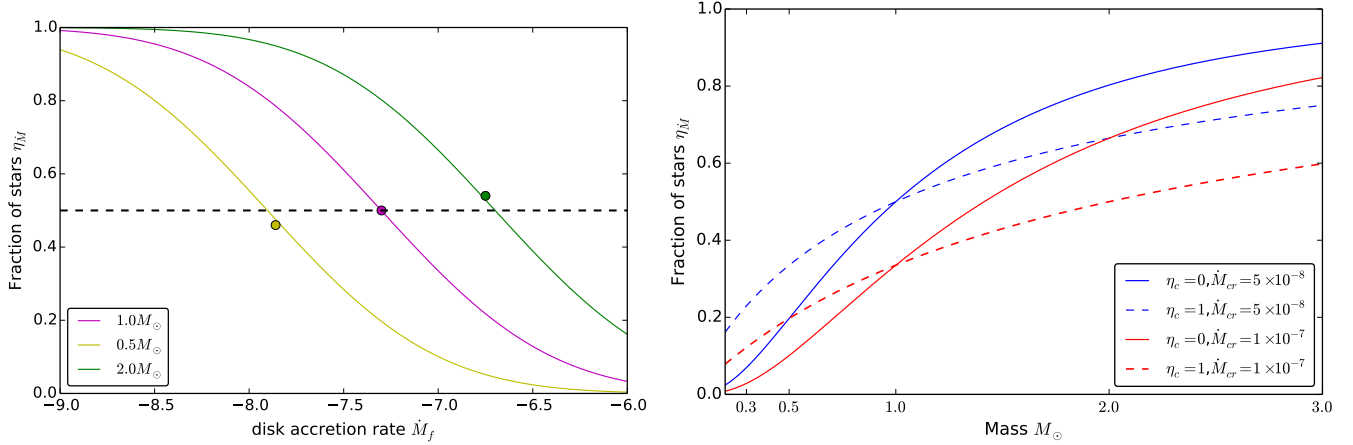


FIG. 4.— **Left:** The  $\eta_M$ - $\dot{M}_g$  correlation for three different stellar masses (yellow, purple, and green lines for  $0.5$ ,  $1$ , and  $2 M_\odot$ , respectively). The black dashed line represents  $\eta_M = 0.5$ , and three colored dots represent the average value of the observed accretion rate for different stellar masses ( $M_* = 0.5, 1$  and  $2 M_\odot$ ) in Garcia Lopez et al. (2006)’s work. **Right:**  $\eta_M$  -  $M_*$  correlation for different  $\eta_c$  (solid and dashed lines for  $\eta_c = 0$  and  $\eta_c = 1$  respectively). The red and blue colors correspond to  $\dot{M}_{cr} = 1 \times 10^{-7} M_\odot \text{ yr}^{-1}$  and  $5 \times 10^{-8} M_\odot \text{ yr}^{-1}$ , respectively. For solar-type stars,  $\eta_M \sim 30\% - 50\%$  as an upper limit for  $\eta$ .

(see Eq (5) and (20) in Ida & Lin 2004a).

In the inner viscously heated region of the disk ( $r < r_{\text{trans}}$ ), the isolation mass is

$$M_{\text{iso}} < \simeq 5 \times 10^3 Z_d^{2/2-3} \eta_{\text{ice}}^{3/2} \alpha_3^{-9/8} m_*^{-5/16} \dot{m}_9^{3/4} \kappa_0^{-3/8} r_{\text{AU}}^{39/16} M_\oplus \quad (11)$$

(this expression corrects a normalization error in Equation 25, Paper II). The outer irradiated region of the disk ( $r > r_{\text{trans}}$ ) is generally outside the snow line (GL07) such that  $\eta_{\text{ice}} = 4$  and

$$M_{\text{iso}} > = 10^{3Z_d/2-2} m_*^{13/28} \dot{m}_9^{3/2} l_*^{-3/7} \alpha_3^{-3/2} r_{\text{AU}}^{39/28} M_\oplus \quad (12)$$

is relatively large due to the condensation of the volatile ices.

If the embryos’ size  $R_p \simeq (M_p/M_\oplus)^{1/2.06} R_\oplus$  (Lissauer et al. 2011),  $\tau_{c,\text{acc}}$  would be a weakly increasing function of  $M_p$  but strongly correlated with  $r$ . In the inner disk region  $\tau_{c,\text{acc}}(M_{\text{iso}}, r < r_{\text{trans}}) \propto r^{7/8} \ll \tau_{\text{dep}}$ , and beyond the transition radius  $\tau_{c,\text{acc}}(M_{\text{iso}}, r > r_{\text{trans}}) \propto r^{11/7} \sim \tau_{\text{dep}}$ . In these regions, embryos acquire their isolation mass. But at very large disk radii (*e.g.*,  $r > 10$  AU),  $\tau_{c,\text{acc}}(M_{\text{iso}}) > \tau_{\text{dep}}$ , so that their growth to dynamical isolation may not be completed before disk gas is depleted (Ida & Lin 2004a).

Recent models also suggest that the embryos could form inside-out at either the inner edge of the dead zone (Chatterjee & Tan 2014) or the magnetic cavity boundary (Li et al. 2016). At these locations, gas pressure in the disk attains local maxima and its azimuthal speed reaches the local Keplerian value. Consequently, pebbles are stalled there as their orbital decay due to aerodynamic drag from upstream (*i.e.*, at large radii). Although disruptive impacts provide growth barriers for meter-size pebbles, collisional fragments remain in the proximity of these specific radii. The accumulation of these building blocks eventually leads to gravitational instability and formation of planetesimals. Subsequent cohesive mergers lead to the emergence of embryos. When their masses increase to several  $M_\oplus$ , they undergo rapid outward type

I migration. Through this mechanism, we anticipate the rapid formation of a population of super-Earth embryos. We still adopt the isolation mass formula from Ida & Lin (2004a) in the following analytical approach; the  $M_{\text{iso}} - m_*$  correlation is robust, but the  $M_{\text{iso}} - \Sigma_d$  relation may not be quantitatively valid any more. Nevertheless,  $M_{\text{iso}}$  approximately equals to  $M_{\text{opt}}$  within a reasonable range of parameters.

While the formation of embryos is discussed elsewhere, we focus here on their tidal interaction with the disk during their growth. From Equation (4), the type I migration time scale is given by

$$\tau_I \equiv \frac{r_p}{\dot{a}} = \left( \frac{h^2}{2f_a} \right) \left( \frac{M_*}{\Sigma_g r^2} \right) \left( \frac{M_*}{M_p} \right) \left( \frac{P}{2\pi} \right) \text{yr} \quad (13)$$

where  $h = H/r$  is the aspect ratio and  $H$  is the thickness of the disk. In the viscously heated inner region, embryos undergo outward type I migrate on a time scale

$$\begin{aligned} \tau_{I<}(M_p) &\simeq (0.62 M_\oplus / f_a M_p) m_*^{3/4} \alpha_3^{1/2} \kappa_0^{1/2} r_{\text{AU}}^{-1/4} \text{Myr} \\ &\simeq \left( \frac{123 M_{\text{iso}}}{f_a M_p} \right) 10^{-3Z_d/2} \eta_{\text{ice}}^{-3/2} \alpha_3^{13/8} m_*^{17/16} \kappa_0^{7/8} \dot{m}_9^{-3/4} r_{\text{AU}}^{-43/16} \text{Myr}. \end{aligned} \quad (14)$$

Embryos grow and reach their local isolation mass provided that  $\tau_{c,\text{acc}}(M_{\text{iso}}) < \tau_{I<}(M_{\text{iso}})$ . But the isolation mass increases with  $\Sigma_d$  as more pebbles accumulate. When embryos attain masses  $M_p$  with  $\tau_{c,\text{acc}}(M_{\text{iso}}) > \tau_{I>}(M_{\text{iso}})$ , they would migrate outward.

Embryos may also form in special disk locations far from their central stars such as the condensation/evaporation boundary (Cuzzi & Zahnle 2004; Kretke & Lin 2007; Ros & Johansen 2013). In the outer irradiated region embryos undergo inward type I migration on a time scale

$$\begin{aligned} \tau_{I>}(M_p) &\simeq (3.97 / f_a) (M_\oplus / M_p) m_*^{-2/7} \dot{m}_9^{-1} l_*^{4/7} \alpha_3 r_{\text{AU}}^{8/7} \text{Myr} \\ &\simeq (397 / f_a) (M_{\text{iso}} / M_p) 10^{-3Z_d/2} \alpha_3^{5/2} m_*^{-3/4} l_* \dot{m}_9^{-5/2} r_{\text{AU}}^{-1/4} \text{Myr}. \end{aligned} \quad (15)$$



In this paper, we consider both possibilities by placing an initial convoy of super-Earth embryos in the inner viscously heated and outer irradiated regions. They migrate extensively and may get trapped at the trapping radius separated by different heating sources. Regardless of their initial spacing, the convergent migration eventually gathers them toward to relatively small separation nearly the trapping radius. We could assume a range of values and start our simulations at that typical time (this is not the time embryos formed but the time embryos approach close to  $r_{\text{trap}}$ ). We will demonstrate the effect of different separations on the final outcome in section 4.2.

### 3.2. From Embryos to Cores

The migration time scales (Eq. 14 and 15) are determined by the sum of differential Lindblad and corotation torque through the magnitude of the efficiency factor  $f_a$  (PBK10, 11). In the irradiated outer region, both torques lead to inward migration. In the viscously heated inner region, embryos with

$$M_{\text{opt}} \simeq m_*^{13/48} \dot{M}_9^{7/12} \alpha_3^{3/8} \kappa_0^{7/24} r_{\text{AU}}^{-7/48} M_{\oplus} \quad (16)$$

experience a maximum-strength, unsaturated corotation torque that is stronger than the differential Lindblad torque and it induces to an outward migration (see Eq [16] in Paper II). The corotation torque for embryos with  $M_p \ll M_{\text{opt}}$  or  $M_p \gg M_{\text{opt}}$  is saturated (weakened) and falls below the differential Lindblad torque. The ratio between the upper and lower mass range for outward migration is  $\sim (2h)^{-2/3}$  which is a few. This mass range would be more extended if the disk had a more complicated layer structure (Kretke & Lin 2012).

Embryos with  $M_p \sim M_{\text{opt}}$  migrate and converge toward the trapping radius located at

$$r_{\text{trans}} \simeq 0.26 m_*^{0.74} l_*^{-0.41} \dot{m}_9^{0.72} \alpha_3^{-0.36} \kappa_0^{0.36} \text{AU} \quad (17)$$

(see Eq. 14 in Paper II) on time scales  $\tau_{I<}(M_{\text{opt}})$  (from the inner region) or  $\tau_{I>}(M_{\text{opt}})$  (from the outer region) (see Eq. 14 and 15).

The local isolation mass around the transition radius may be substantially enhanced (with a relatively large  $Z_d$ ) by a local concentration of trapped building-block embryos (Liu et al. 2015). We also showed (in Eq. 32, Paper II) that convergent embryos in disks with  $\dot{m}_9 < \dot{m}_{9 \text{ res}}$  where the critical magnitude is

$$\dot{m}_{9 \text{ res}} \simeq 6 f_{\text{res}}^{0.95} m_*^{-1.33} \alpha_3^{0.97} \kappa_0^{-0.026} l_*^{0.70}, \quad (18)$$

tend to trap each other on their mutual MMRs and form a convoy of super-Earths. The magnitude of a dimensionless coefficient  $f_{\text{res}}$  is of order a few, and it is smaller for 3:2 than 2:1 MMR (Papers I & II). In disks with  $\dot{m}_9 > \dot{m}_{9 \text{ res}}$ , embryos can bypass their MMR barrier, enter into each other's feeding zone, undergo close encounters and coalesce.

Convergent migration to  $r_{\text{trans}}$  enhances the local concentration of building-block material. Provided that  $\tau_{\text{c,acc}}(M_{\text{opt}})$  is substantially smaller than  $\tau_{\text{dep}}$ , the trapped embryos grow to the optimum mass at  $r_{\text{trans}}$  with

$$M_{\text{opt}}(r_{\text{trans}}) \simeq 1.2 m_*^{0.16} \dot{m}_9^{0.48} \alpha_3^{0.43} \kappa_0^{0.24} l_*^{0.06} M_{\oplus}. \quad (19)$$

Embryos' growth beyond a few times  $M_{\text{opt}}(r_{\text{trans}})$  would lead to corotation torque saturation and orbit decay.

If  $M_{\text{opt}}(r_{\text{trans}}) > M_c$ , large cores that emerged out from convergent embryos can also retain and accrete gas around the trapping radius.

Close encounters between optimum-mass and residual embryos trapped at  $r_{\text{trans}}$  excite their eccentricity and widen their semimajor-axis separation. The extent of orbital change increases with the ratio between embryos' surface escape ( $V_e$ ) and the Keplerian ( $V_k$ ) speed at  $r_{\text{trans}}$ ,

$$f_V \equiv V_e(M_{\text{opt}})/V_k(r_{\text{trans}}) \quad (20)$$

From Equation (17) and (19) we find

$$f_V \simeq 0.2 m_*^{-0.09} \dot{m}_9^{0.48} \alpha_3^{-0.07} l_*^{-0.19} \kappa_0^{0.24}. \quad (21)$$

Encounters with a small or moderate value of  $f_V (\ll 1)$  do not strongly modify the orbits of interacting embryos. Their eccentricity is rapidly damped as they resume their convergent type I migration—from a scattered location  $r_{\text{scat}}$  inside and outside  $r_{\text{trans}}$  to its proximity—on time scales of  $\tau_{I<}(M_p, r_{\text{scat}} < r_{\text{trans}})$  and  $\tau_{I>}(M_p, r_{\text{scat}} > r_{\text{trans}})$  where

$$\tau_{I<} \simeq \left( \frac{0.62 m_*^{23/48} \alpha_3^{1/8} \kappa_0^{5/24}}{f_a \dot{m}_9^{7/12}} \right) \left( \frac{M_{\text{opt}}}{M_p} \right) r_{\text{scat,AU}}^{-5/48} \text{Myr}. \quad (22)$$

$$\tau_{I>} \simeq \left( \frac{4 m_*^{-187/336} \alpha_3^{5/8} l_*^{4/7}}{f_a \dot{m}_9^{19/12}} \right) \left( \frac{M_{\text{opt}}}{M_p} \right) r_{\text{scat,AU}}^{1.3} \text{Myr} \quad (23)$$

where  $r_{\text{scat,AU}} = r_{\text{scat}}/1\text{AU}$ .

### 3.3. Onset of Gas Accretion

In disks with  $M_{\text{opt}}(r_{\text{trans}}) > M_c (\sim 10 M_{\oplus})$ , efficient gas accretion proceeds on a Kelvin-Helmholtz time scale (Pollack et al. 1996; Ikoma et al. 2000; Ida & Lin 2004a)

$$\tau_{\text{KH}} \simeq \kappa_{\text{acc}}(M_{\oplus}/M_p)^3 \text{Gyr}. \quad (24)$$

Under the assumption that the opacity of the accreted gas  $\kappa_{\text{acc}} \sim \kappa_0$ ,

$$\tau_{\text{KH}}(M_{\text{opt}}, r_{\text{trans}}) \simeq 0.58 \kappa_0^{0.28} m_*^{-0.48} \dot{m}_9^{-1.44} \alpha_3^{-1.29} l_*^{-0.18} \left( \frac{M_{\text{opt}}}{M_p} \right)^3 \text{Gyr} \quad (25)$$

for  $M_p \simeq M_{\text{opt}}$  at  $r_{\text{trans}}$ . In the limit of  $\dot{M}_g = 10^{-7} M_{\odot} \text{yr}^{-1}$ ,  $M_{\text{opt}}(r_{\text{trans}}) \sim M_c$  and  $\tau_{\text{KH}} \simeq 0.6 \text{Myr}$ , growth beyond  $M_{\text{opt}}$  would further reduce  $\tau_{\text{KH}}$  and increase the gas accretion rate onto the cores.

### 3.4. Core-formation threshold around stars with different $M_*$ and $Z_*$

In order to determine the  $\eta_J$ - $M_*$  and  $\eta_J$ - $Z_*$  correlations, we use Equation (5) to replace  $\dot{M}_g$  with a fiducial average value  $\dot{M}_a$  and assume that (1)  $l_* \propto m_*^2$ ; (2)  $\eta_b = 2$ , i.e.,  $\dot{m} \propto m_*^2$ ; and (3)  $Z_d$  is independent of  $M_*$ . Based on Eq. (17, 22, 25, 19, 18 and 21), we summarize here:

$$M_{\text{iso}<} \simeq 5 \dot{m}_{a\odot 9}^{3/4} 10^{3Z_d/2-3} \eta_{\text{ice}}^{3/2} m_*^{19/16} \kappa_0^{-3/8} r_{\text{AU}}^{39/16} M_{\oplus}, \quad (26)$$

$$\tau_{I<}(M_{\text{opt}}) \simeq 0.62 \dot{m}_{a\odot 9}^{-7/12} m_*^{-33/48} \alpha_3^{1/8} \kappa_0^{5/24} r_{\text{AU}}^{-5/48} \text{Myr}, \quad (27)$$

$$r_{\text{trans}} \simeq 0.26 \dot{m}_{a\odot 9}^{0.72} m_*^{1.36} \alpha_3^{-0.36} \kappa_0^{0.36} \text{AU} \quad (28)$$

$$M_{\text{opt}}(r_{\text{trans}}) \simeq 1.2 \dot{m}_{a\odot 9}^{0.48} m_*^{1.24} \alpha_3^{0.43} \kappa_0^{0.24} M_{\oplus}. \quad (29)$$

$$\dot{m}_{9 \text{ res}} \simeq 6 f_{\text{res}}^{0.95} m_*^{0.07} \alpha_3^{0.97} \kappa_0^{-0.026} \quad (30)$$

$$\tau_{\text{KH}}(M_{\text{opt}}, r_{\text{trans}}) \simeq 0.58 \dot{m}_{a\odot 9}^{-1.44} m_*^{-3.72} \alpha_3^{-1.29} \kappa_0^{0.28} \text{Myr}. \quad (31)$$

$$f_V \simeq 0.2 m_*^{0.49} \alpha_3^{-0.07} \kappa_0^{0.24} \dot{m}_{a\odot 9}^{0.48}. \quad (32)$$

where  $\dot{m}_{a\odot 9} = \dot{M}_{a\odot}/10^{-9} M_{\odot} \text{ yr}^{-1}$  and  $\dot{M}_{a\odot}$  (average accretion rate for solar-mass protostars) is in the range of  $\sim 1 - 5 \times 10^{-8} M_{\odot} \text{ yr}^{-1}$  during the T Tauri phase.

It is often assumed that the amount of heavy elements in the disk (or  $\Sigma_d$ ) is proportional to  $M_*$  such that embryos' growth timescale decreases and isolation mass increases with  $M_*$ . The supercritical cores are easier to form around relatively massive stars, which is in agreement with the  $\eta_J$ - $M_*$  correlation.

However,  $M_{\text{iso}}$  also increases with  $Z_d$  which may be enhanced by the convergent migration. The luminosity of T Tauri stars  $L_* \propto M_*^2$  (D'Antona & Mazzitelli 1994). Taking into account of this dependence, these results imply a threshold increase in  $\eta_J$  for relatively massive stars because

1.  $r_{\text{trans}} \propto m_*^{1.36}$  and is beyond the snow line where volatile ices contribute to both  $\eta_{\text{ice}}$  and  $\kappa_0$  of the building-block material;
2.  $M_{\text{iso}} \propto m_*^{19/16}$  and is larger than  $M_c$  so that efficient gas accretion may be initiated;
3.  $\dot{m}_{9 \text{ res}} \propto m_*^{0.07}$  and  $\dot{m}_a \propto m_*^2$  so that the MMR barriers may be bypassed;
4.  $M_{\text{opt}} \propto m_*^{1.25}$  and is larger than  $M_c$ ;
5.  $\tau_{\text{KH}} \propto m_*^{-3.72}$  and is comparable to or less than  $\tau_{\text{dep}}$ .

Note that  $\dot{m}_{9 \text{ res}}$  is essentially independent of the stellar mass while  $\dot{M}_a \propto M_*^2$  and  $L_* \propto M_*^2$ , and a larger fraction of embryos around relatively massive ( $M_* \sim 2 M_{\odot}$ ) stars are able to bypass the MMR barrier and converge onto crossing orbits near  $r_{\text{trans}}$ . These embryos undergo close encounters with each other, including large-angle deflection and physical collisions. Scattered embryos repeatedly return to  $r_{\text{trans}}$  until eventually they collide and merge into supercritical cores. Since  $M_{\text{opt}}(r_{\text{trans}}) > M_c (\sim 10 M_{\oplus})$  and  $\tau_{\text{KH}}(M_{\text{opt}}, r_{\text{trans}})$  decreases rapidly with stellar mass, rapid gas accretion onto relatively massive retained cores promotes the formation of gas giants around intermediate-mass and massive stars.

In disks with  $\dot{M}_g \sim \dot{M}_a$ , changes in the orbital properties of the scattered embryos due to close encounters at  $r_{\text{trans}}$  increase with the mass of the host stars. Equation (21) implies that  $f_V \propto m_*$ . In the large  $f_V (\geq 1)$  limit, most embryos are either ejected or scattered to distances far well beyond  $r_{\text{trans}}$  where  $\Sigma_g$  is low and  $\tau_{I>}$  becomes longer than  $\tau_{\text{dep}}$  (Eq. 15). This consideration introduces the possibility of transporting cores to large distances and the formation of long-period gas giants. We defer further discussion on multiple-planet formation in evolving disks to subsequent papers in this series.

#### 4. FORMATION OF CRITICAL CORES AMONG DIFFERENT STELLAR MASS SYSTEMS

##### 4.1. standard case

In this section, we present numerical models to verify the analytic results presented in the previous section. We investigate the role of disk accretion rate ( $\dot{M}_g$ ) and stellar mass ( $M_*$ ) on assembling of supercritical cores with our Hermite-Embryo code.

In principle, the disk accretion rates may be extraordinarily high and  $M_{\text{opt}} \gg 10 M_{\oplus}$  during the brief ( $\sim 10^5$  yr) embedded phase when their central stars acquire most of their masses. However, if disks have retained a large fraction of their initial angular momentum content and the disk wind is not the dominant mechanism for mass and angular momentum removal, the Class I phase disks would probably be much more compact and hotter than typical protoplanetary disks around T Tauri stars. Although grains may condense in the outer region of rapidly evolving disks with very high  $\dot{M}_g$ , it is not clear whether there is adequate time for them to coagulate and grow into embryos with isolation masses of a few  $M_{\oplus}$ .

The magnitude of  $\dot{M}_g$  decreases with time, and that of the corresponding optimum mass ( $M_{\text{opt}}$ ) for the trapped embryos (Eq. 29) is well below  $M_c$  in the transitional or debris disks. Therefore, the necessary condition for core formation (*i.e.*, the magnitude of  $\eta_J$ ) is during the early Class II stage of disk evolution. Following Paper II, we start our simulations when the average accretion rate  $\dot{M}_a$  is comparable to that of classical T Tauri stars.

We limit model parameters to those in Table 1. For simplicity, equal-mass embryos are treated here with  $M_p$  in the range that is consistent with the analytical estimation of Equation (11) and (12). We assume perfect coalescence with the conservation of total mass and angular momentum when either (1) the separation of two embryos is smaller than the sum of their physical radii estimated by Lissauer et al. (2011) or (2) they form a close-in binary with a common orbital period less than 10 days. The realistic super-Earth-mass embryos contain a modest envelope, and the drag of accreted gas would increase the capture cross section during close encounters (Ormel & Kobayashi (2012)). And separation of such pairs shrinks, so they eventually merge due to their tidal interaction with the disk and common envelope (Baruteau et al. 2011). We specify criteria (2) for both physical consideration and computational idealization. Our simulation results show that almost 90% of mergers are due to criteria (1). We examine the embryos' evolution under different disk accretion ( $\dot{M}_g$ ) and stellar mass ( $M_*$ ) in Figure 5. Nine panels are shown with  $\dot{M}_g = 10^{-8}$ ,  $5 \times 10^{-8}$ , and  $10^{-7} M_{\odot} \text{ yr}^{-1}$  (left to right panels) and  $M_* = 0.5, 1.0$ , and  $2.0 M_{\odot}$  (top to bottom panels). Six  $5 M_{\oplus}$  embryos are embedded on each side of the trapping radius with  $10 R_R$  initial separation. We also verify the non-gap-opening criterion (Equation [19] in Paper II) for parameter space ( $M_*, \dot{M}_g$ ) adopted here and ensure the type I migration assumption in our simulations is justified. In a layered disk, midplane viscosity becomes much smaller than that of the surface layer due to the limited penetration depth of stellar ionizing photons. As demonstrated in Kretke & Lin (2012) and Paper II, the lower mass range for outward migration is roughly  $(2h)^{2/3} M_{\text{opt}}$ , which increases with viscosity through  $M_{\text{opt}}$ 's dependence on  $\alpha$  (see Eq 16). In

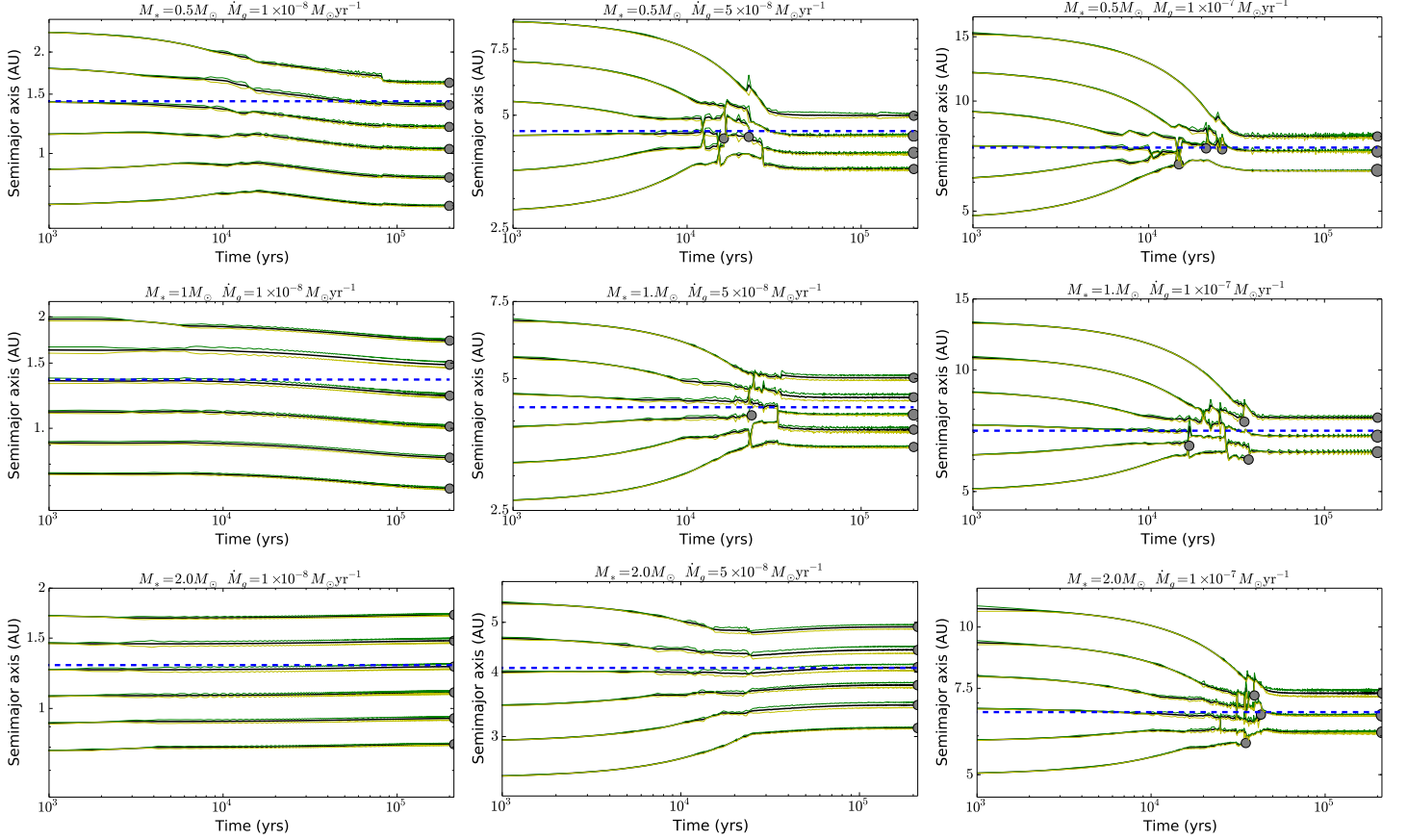


FIG. 5.— Mutual interaction between embryos and their natal disks for different stellar masses  $M_*$  and disk accretion rates  $\dot{M}_g$ . The black lines trace the evolution of embryos' semimajor axes and the blue dashed line indicates the location of  $r_{\text{trap}}$ . The green and yellow lines are embryos' apocenter and pericenter distance. Disk parameters are chosen to be those of model A. All systems contain six  $5 M_\oplus$  embryos that are initially distributed on either side of the trapping radius with  $10 R_R$  separation. The accretion rate ( $\dot{M}_g = 10^{-8} M_\odot \text{yr}^{-1}$ ,  $5 \times 10^{-8} M_\odot \text{yr}^{-1}$  and  $10^{-7} M_\odot \text{yr}^{-1}$ ) increases from left to right panels. The stellar mass ( $M_* = 0.5, 1$  and  $2 M_\odot$ ) increases from top to bottom panels.

TABLE 1  
MODELS WITH A RANGE OF STELLAR MASS AND DISK ACCRETION RATE

Models	Mass of the Planets ( $M_\oplus$ )	Number of Planets	Initial Separation $k_0$ ( $R_R$ )	Opacity $\kappa_0$
Series 1	5	6	7	1
Series 2	5	6	10	1
Series 3	5	6	12	1
Series 4	5	6	15	1
Series 5	3	10	10	1

Model	Stellar Mass ( $M_\odot$ )	Accretion Rate $\dot{M}$ ( $M_\odot \text{yr}^{-1}$ )
Model A	2.0	$10^{-8}$
Model B	2.0	$5 \times 10^{-8}$
Model C	2.0	$10^{-7}$
Model D	1.0	$10^{-8}$
Model E	1.0	$5 \times 10^{-8}$
Model F	1.0	$10^{-7}$
Model G	0.5	$10^{-8}$
Model H	0.5	$5 \times 10^{-8}$
Model J	0.5	$10^{-7}$

this section, we adopt the prescription and fiducial values of model C in Paper II, in which  $\alpha_\nu = \alpha_M$  when  $R_R < R_{\text{dz}}$  and  $\alpha_\nu = \alpha_M + (\alpha_H - \alpha_M) \left( \frac{(R_R/R_{\text{dz}})^2 - 1}{(R_R/R_{\text{dz}})^2 + 1} \right)$  when  $R_R > R_{\text{dz}}$ .  $R_R$  is the planetary Roche radius, and the size of the dead zone is  $R_{\text{dz}} = \dot{H}(r) \Sigma_g(r) / \Sigma_\eta$ , where  $\alpha_H = 10^{-3}$ ,  $\alpha_M = 1.4 \times 10^{-4}$  and  $\Sigma_\eta = 10^4 \text{gcm}^{-2}$ . This

condition ensures that  $3 - 5 M_\oplus$  are within the optimal mass range for outward migration in disks around stars with  $M_* = 0.5 M_\oplus - 2 M_\oplus$ .

The orbital evolution of embryos around an  $M_* = 0.5 M_\odot$  central star is displayed in the first row of Figure 5. The group of embryos undergo convergent migration

with a slow pace in a low-accretion disk and with a fast pace in high-accretion disk. In the low accretion rate model ( $\dot{M}_g = 10^{-8} M_\odot \text{yr}^{-1}$  for top left panel), embryos' migration is stalled as they capture each other into their mutual MMR and evolve into chains of low-mass planet systems. This result is consistent with the Kepler's data, which indicate the common existence of multiple super-Earth systems with  $M_p < M_c$  and  $M_s > M_c$  (§2.1).

In the intermediate and high accretion rate models ( $\dot{M}_g = 5 \times 10^{-8} M_\odot \text{yr}^{-1}$  for top middle panel and  $\dot{M}_g = 10^{-7} M_\odot \text{yr}^{-1}$  for top right panel), orbital crossing between embryos happens repeatedly after  $10^4$  yrs and some eventually lead to a merger. The asymptotic mean separations between neighboring residual embryos in above three runs are around  $6.2R_R$ ,  $3.5R_R$  and  $3R_R$  respectively. These results indicate that the lack of gas giants around M stars may be associated with their relatively low  $\dot{M}_a$  in gaseous disks rather than their smaller  $M_s$ , the total supply of building-block material.

Similar results (middle and bottom rows) are also found for the solar-type and intermediate-mass stars (with  $M_* = 1$  and  $2M_\odot$ ). For the same  $\dot{M}_g$ , the location of the trapping radius is essentially independent of  $m_*$  (see Eq 17) (from top to bottom rows). However,  $r_{\text{trans}}$  increases with  $\dot{M}_g$  (from left to right panels) for the same  $M_*$ . These numerical results of type I migration timescales are also consistent with the estimation of Equation (14) and (15).

At a similar  $\dot{M}_g (\sim 5 \times 10^{-8} M_\odot \text{yr}^{-1})$ , the disk torque is sufficiently strong for embryos to cross each orbit and merge together to form critical cores. The formation of supercritical cores appears to be significantly dependent on gas accretion rate (from left to right panel), but the correlation for stellar mass is shown to be relatively weak (from top to bottom panels). These results may imply that the value of  $\eta_c$  in  $\dot{M}_f$  (Eq. [8]) is close to zero, which will be further discussed in the next subsection.

Bitsch & Kley (2010) showed that corotation torque would also be saturated due to non-negligible eccentricity. This effect is modest as eccentricity is smaller than 0.03 and the embryo can still undergo outward migration (their Figure 3). In our simulations, the eccentricities maintain a relatively low equilibrium value of  $\sim 0.02$  except for close encounters. Corotation torque would be weakly suppressed due to nonzero eccentricity during the convergent migration. However, the other neglected work here is additional stochastic torques due to the fluctuation nature of disk turbulence. Pierens et al. (2013) proved that these random stochastic torques can disrupt the resonant configurations and enhance the growth of massive cores. We expect that our outcomes will be compromised when both physical processes are taken into account, and the main conclusion of the paper is still convincing.

#### 4.2. Dispersion in the critical accretion rate

In addition to the disk accretion rate and stellar mass, embryos' migration rate is determined by the saturation of their corotation torque from  $f_a$  (Eq. 13), Consequently,  $\dot{M}_f$  is a function of  $M_p$  through  $f_a$  (see §3.2). We now assess the dispersion in the threshold accretion rate for a range of  $M_p$  values.

Using the Hermite-Embryo code, we carry out three series of simulations (see Table 1) with either six  $5 M_\oplus$  or ten  $3 M_\oplus$  embryos and various initial separations (7, 10, 12 and  $15 R_R$ ). Total planet mass is identical ( $30 M_\oplus$ ) for all series. Embryos' eccentricity is chosen from Rayleigh distribution with a mean value  $e_0 = 0.02$ , and they are all in coplanar orbits with random orientations and phase angles, and with initial locations interior and exterior to the trapping radius. In each series, we perform 9 different models, with three different  $M_*(= 0.5, 1, 2 M_\odot)$  and  $\dot{M}_g$  ( $10^{-8}, 5 \times 10^{-8}, 10^{-7} M_\odot \text{yr}^{-1}$ ).

Resonant capture, orbit crossing, and physical collisions are stochastic processes. In order to boost the statistical significance of our results, we simulate 5 independent runs with slightly different initial semimajor axes and orbital phases in each model. For series 1, 2, and 5, we show, in the top, middle, and bottom panels of Figure 6, the mean asymptotic separation  $k_0$  (normalized by  $R_R$ ). Models with  $2 M_\odot$ ,  $1 M_\odot$  and  $0.5 M_\odot$  are respectively represented by red circles, green pentagons and yellow rectangles.

For a given set of model parameters (such as  $M_*$  and  $\dot{M}_g$ ), variations in the initial conditions generate a limited range of  $k_0$  (indicated by the error bar). We find that embryos final mean separation is dependent on the initial spacing only for the low-accretion cases (e.g.,  $\dot{M}_g < 2 - 3 \times 10^{-8} M_\odot \text{yr}^{-1}$ ). In disks with relatively high accretion rates, they undergo fast migration pace, bypass their mutual MMR barriers and attain similar final spacing with modest variations. Similarities between series 1 – 4 results for  $\dot{M}_g > 3 \times 10^{-8} M_\odot \text{yr}^{-1}$  indicate that convergent migration gathers embryos toward  $r_{\text{trans}}$  along similar paths regardless of their initial configurations. Comparison between series 1 and 5 indicates that provided  $M_p$  is comparable to the optimum mass  $M_{\text{opt}}$  calculated in Eq. [16], the asymptotic  $k_0$  and embryos' collision probability are insensitive to the embryos' initial isolated mass. In all cases, these asymptotic values of  $k_0$  are reached well within the gas depletion time scale  $\tau_{\text{dep}}$ .

In the limit of small  $\dot{M}_g (\leq 10^{-8} M_\odot \text{yr}^{-1})$ , embryos capture each other onto their MMRs. But  $k_0$  is a decreasing function of  $\dot{M}_g$  for all 3 values of  $M_*$ . The black solid lines in Figure 6 denote the critical separation ( $k_0 = 5$ ) less than which neighboring embryos perturb and cross each other's orbits within a few times  $10^4$  yr (Zhou et al. 2007). Subsequently, they undergo frequent close encounters, collide and merge into supercritical cores. Since the orbit crossing time is a rapidly increasing function of  $k_0$  (see §3.2), we approximate  $\dot{M}_f$  by the magnitude of  $\dot{M}_g$  which leads to  $k_0 = 5$ . Similarities between the three panels indicate that our results are insensitive to the initial separation and mass of embryos around the optimum value for the parameter ranges explored here. The approximate values (i.e.,  $\dot{M}_g$  which leads to  $k_0 = 5$ ) of  $\dot{M}_f$  are 2.7, 4.0,  $6.3 \times 10^{-8}$  for  $M_* = 0.5, 1.0, 2.0 M_\odot$  respectively (see top panels of Fig. 6). These results can be fitted to Equation (8) with  $\eta_c \sim 0.6$ . But the analytic approximation in Equation (30) indicates  $\eta_c \sim 0.07$ . The minor  $\eta_c$  difference is caused by the condition we used for the analytic approximation and numerical computation

of the threshold orbit crossing condition.

The critical accretion rate (Eq (30)) is derived from Murray & Dermott (1999), which requires that the time scale for the differential migration ( $\tau_{\Delta a}$ ) between planet pairs through their characteristic libration width is longer than the resonant angle libration time scale ( $\tau_{lib}$ ). For the libration time scale, it relies on a coefficient factor  $f_{res}$  which is a function of the semi-axis ratio between the two planets, e.g.  $f_{res}$  is smaller for 4 : 3 than 3 : 2 resonance. Ogihara & Kobayashi (2013) indicates that this coefficient factor also depends on the outer-to-inner planet mass ratio when the value is larger than 0.1. The difference in our cases is that  $f_{res}$  is also  $M_p$  dependent due to the saturation of corotation torque, so we are only interested in the limited mass range close to  $M_{opt}$ . They simulated two planets' migration and found that for equal-mass planets the critical migration time scale to pass through 2 : 1 resonance is one order of magnitude shorter than that for a very small mass ratio. In our work, the initial separation between embryos is much smaller than that in 2 : 1 resonance. According to their simulation results (see the Table 3 in Ogihara & Kobayashi (2013)), the critical migration time scale is only reduced by a factor of 2 for 4 : 3 and 5 : 4 MMRs when the planets have equal mass. The situation is suspected to be more complicated, and resonance configurations would also be disrupted when the number of embryos is large (Pierens et al. 2013). The exploration of  $M_p$  dependence on resonance capture (Eq 30) is not a proper and prior task for this study. At least for the numerical experiments implemented here, we find the planet mass is insensitive to embryos' collision probability and final asymptotic  $k_0$ .

In the numerical fit to the observed  $\dot{M}_a$  (Eq 5),  $\eta_b \sim 1.3 - 2.0$ . Provided  $\eta_b > \eta_c$ , the actual accretion rate increases with  $M_*$  faster than the threshold accretion rate for inducing embryos to bypass their MMR barriers and cross each other's orbits. Cohesive collisions increase  $M_p$ . The migration of mergers continues to converge around  $r_{tran}$ , provided their  $M_p$  reach  $M_c$  within a relatively short timescale. (§3.2).

The corotation torque is saturated (weakened) for embryos with  $M_p > M_{retain} \simeq (2h)^{-2/3} M_{opt}$  (see §3.2). Values of  $M_{retain}$  are shown in Figure 7. Torque on embryos with  $M_p > M_{retain}$  is dominated by the contributions from differential Lindblad resonances, which generally induce them to migrate inward. The magnitude of  $M_{retain}$  is typically  $\sim 2.2 M_{opt}$  (Paper II), which increases with both  $M_*$  and  $\dot{M}_g$  (see Eq 19). It also decreases with the distance to the central stars (see Eq 16). Around  $M_* = 0.5 M_\odot$ ,  $M_{retain} > M_c$  in the limit  $\dot{M}_g > 3 \times 10^{-8} M_\odot \text{ yr}^{-1}$  (yellow rectangle). Around  $M_* = 2 M_\odot$ ,  $M_{retain} > M_c$  in the limit  $\dot{M}_g > 10^{-8} M_\odot \text{ yr}^{-1}$  (red circle). Together with the condition of threshold accretion rate, these results imply that if  $\dot{M}_g$  is sufficiently large to form critical-mass cores, they would be retained near the trapping radius.

Supercritical cores accrete gas on the time scale  $\tau_{KH}(M_{retain}) (\propto m_*^{-3.72})$  (see Eq 25 in §3.3). Although their  $M_p$  may reach and exceed  $M_{retain}$  during their subsequent gas accretion, they would accrete gas and evolve into gas giants *in situ* if the migration timescale

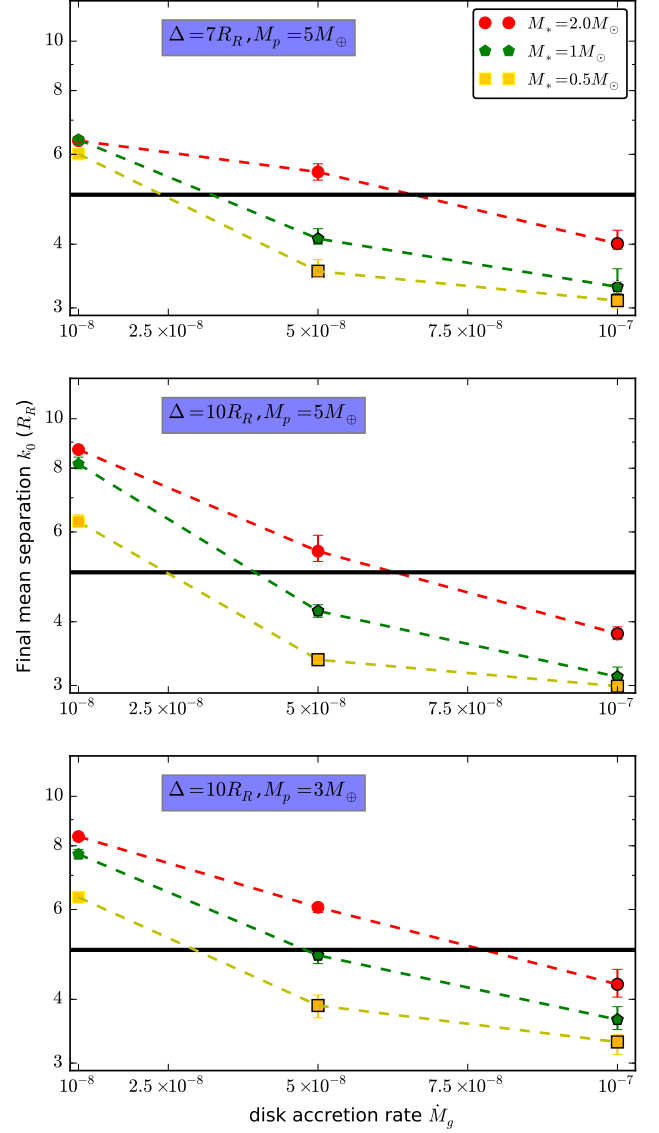


FIG. 6.— Asymptotic mean separation  $k_0$  vs. disk accretion rate  $\dot{M}_g$  for series 1, 2, and 5 (from the top to the bottom panels). Red circles, green pentagons and yellow rectangles represent the models with  $M_* = 2 M_\odot$ ,  $M_* = 1 M_\odot$  and  $M_* = 0.5 M_\odot$ , respectively. Symbols with black borders represent models in which merger occurred during the evolution. Embryos which captured each other in MMR without coalescence are denoted by symbols without borders. The thick horizontal black lines mark the critical final mean separation, *i.e.*  $5R_R$ . If the planets enter into a more compact configuration, dynamical instability would lead to orbit crossing and collisions within  $10^5$  yr.

$\tau_I(M_{retain}) > \tau_{KH}(M_{retain})$ . As they gain mass, proto-gas-giant planets strongly perturb their natal disks by opening up gaps and transit from type I to slow type II migration (Lin & Papaloizou 1986).

In general, critical-mass cores form more readily, are more likely to be retained, and can grow into gas giants more rapidly around relatively massive stars. Quantitatively, the transition from convoys of resonant super-Earths to gas giants occurs in the  $\eta_{\dot{M}}-M_*$  domain between the red and blue lines (represent  $M_{cr} = 1 \times 10^{-7} M_\odot \text{ yr}^{-1}$  and  $M_{cr} = 5 \times 10^{-8} M_\odot \text{ yr}^{-1}$  respectively) in the right panel of Figure 4. This correlation generally

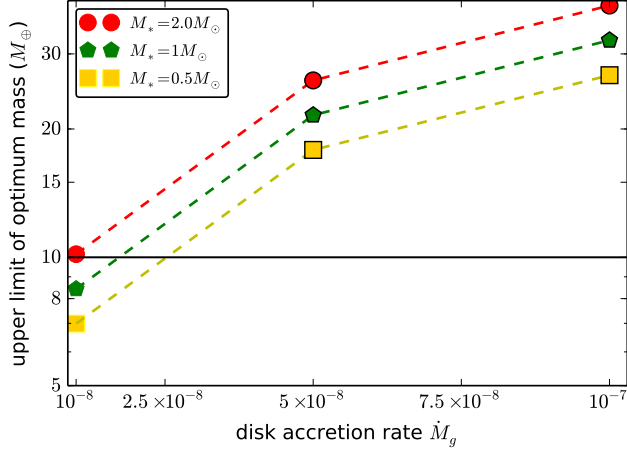


FIG. 7.— Maximum value of optimum planet mass as a function of  $M_*$  and  $\dot{M}_g$ . The critical core mass  $M_c (= 10 M_\oplus)$  is marked by the black line. The red circles, green pentagons, and yellow rectangles represent the maximum mass of the trapped embryos for three stellar masses ( $M_* = 2, 1, 0.5 M_\odot$ , respectively).

agrees with the observed  $\eta_J$ - $M_*$  correlation, though the magnitude of the simulated  $\eta_J$  is somewhat higher than the observed  $\eta_J$  (see further discussions in §5.4).

## 5. FORMATION OF CRITICAL CORES AROUND STARS WITH DIFFERENT METALLICITIES

In this section, we first examine the correlation between  $Z_d$  and  $Z_*$  prescription. Following similar methods from the previous two sections, we determine the dependence of critical  $\dot{M}_f$  on the  $Z_d$  of the disk gas. We then combine these two sets of results to determine the main causes of the observed  $\eta_J$ - $Z_*$  correlations.

Equation (7) indicates that  $\eta_J$  is determined by both the critical accretion  $\dot{M}_f$  for core formation and the actual observed value of the disk accretion rate  $\dot{M}_a$ . We suggest that the average values of opacity  $\kappa_0$ , isolation mass  $M_{\text{iso}}$  and trapping radius  $r_{\text{trans}}$  are increasing functions of  $\Sigma_d$ . These factors affect the magnitude of  $\dot{M}_f$ .

### 5.1. Metallicity of grains and embryos in protostellar disks versus stellar metallicity

In the sequential accretion scenario, heavy elements are not only the building blocks of embryos and cores, but also the main opacity source such that  $\Sigma_d$  determines not only the dynamical evolution of the embryos and cores but also the disk structure. However,  $\Sigma_d$  cannot be directly determined from observations of optically thick protostellar disks. The metallicity of T Tauri stars is also poorly determined such that there are no well-established  $Z_d$ - $Z_*$  correlation or any  $\dot{M}_a$ - $Z_*$  dependence (in contrast to the observed  $\dot{M}_a$ - $M_*$  correlation in Eq. 5). In typical accretion disk models (Hartmann 1998), it is customary to construct a  $\Sigma_g$  distribution and to determine  $\Sigma_d$  based on the assumption that  $Z_d \propto Z_*$  throughout the disk (Laughlin et al. 2004a; Ida & Lin 2005; Mordasini et al. 2012).

Based on the following four circumstantial evidences, we revisit the validity of this assumption.

A1) Perhaps the strongest evidence for  $Z_d \propto Z_*$  is the correlation of abundance distribution between the solar

atmosphere and chondritic meteorites for nearly all refractory elements (Anders & Grevesse 1989). There are clear indications of volatile-element depletion either due to evaporation or inability to condensate.

A2) During their formation, all of the stellar mass content, including H, He, and heavy elements, passes through protostellar disks. Efficient retention of heavy elements in the disk would not only enhance  $Z_d$  but also reduce  $Z_*$  from the protostellar clouds. Upper limits on the iron abundance variation ( $\Delta [\text{Fe}/\text{H}]_* \leq 0.02$ ) among solar-type stars in young stellar clusters (such as Pleiades and IC 4665) (Wilden et al. 2002; Shen et al. 2005) suggest that the total amount of heavy elements and its dispersion in protostellar disks is limited to less than twice that in the solar nebula. They are generally smaller than the range of  $Z_*$  between different open clusters. Metallicity dispersion in planet-hosting binary stars (such as 16 Cyg and XO2) (Ramírez et al. 2011, 2015) can also be interpreted to support the assumption that protostellar disks are formed with  $Z_d \sim Z_*$ .

A3) The typical accretion rate in protostellar disks around solar-type stars is a few times  $10^{-8} M_\odot \text{ yr}^{-1}$ . If their viscous diffusion time scale is comparable to the age (a few Myr) of their central stars, the mass of gas  $M_g$  in these disks would be comparable to or a few times larger than that of the MMSN (i.e., a few times  $10^{-2} M_\odot$ ). Total mass ( $M_z$ ) in millimeter-size (both volatile and refractory) grains in these disks (Beckwith et al. 1990) is comparable to or a few times that of heavy elements in the MMSN model. The ratio  $M_z/M_g (\sim 10^{-2})$  of T Tauri stars is comparable to that in the Sun.

A4) In §2.3, we indicate that  $\dot{M}_d \propto M_*^{\eta_b}$  and  $\eta_b \sim 1.3 - 2.0$  (Eq. 5). Most of the gas is distributed in the outer irradiated region where  $\Sigma_g \propto \dot{M}_d$  (GL07). Recent millimeter observation (Andrews et al. 2013) suggests that  $\Sigma_d \propto M_*$ . These inferred ( $\Sigma_g$ - $M_*$  and  $\Sigma_d$ - $M_*$ ) correlations suggest that the ratio  $\Sigma_d/\Sigma_g$  may vary significantly with  $M_*$ .

Bear in mind that the millimeter continuum observations of  $\Sigma_d$  only determine the heavy-element content in the millimeter-size range. We do not have any reliable information on the abundant small-size grains or large-size planetesimals. Due to the lack of constraints on the gas/dust depletion factors, it is also difficult to extract quantitative information on both  $\Sigma_d$  and  $\Sigma_g$  from spectroscopic (CO) observations. Although  $M_*$  can be directly determined from photometric observations, we also do not have any reliable data on the metallicity of the infant host stars  $Z_*$ . Nevertheless, from the above circumstantial evidences, we infer, within an order of magnitude, the ratio  $\Sigma_d/\Sigma_g$  in protostellar disks is comparable to heavy elemental fraction in their central stars. We now assess the dispersion in the  $Z_d$ - $Z_*$  correlation in terms of theoretical considerations.

B1) During the formation and early phase of their evolution when disks are more compact, hotter, and vigorously turbulent, the gas accretion rate is high ( $> 10^{-6} M_\odot \text{ yr}^{-1}$ ) and dust grains are well coupled to the dense disk gas, it is likely that  $Z_d \simeq Z_*$ . At that epoch, the dust destruction radius  $r_{\text{ref}}$  extends to a large fraction of the disk so that grains may only be available in the outer disk regions (beyond 1 AU). The rapid evolution of the disk may also limit the available time window (a few times



$10^5$  yr) for embryos to grow to a few  $M_\oplus$ .

B2) During the main evolution stage of protostellar disks, several physical processes may induce the decoupling of gas and solid, and lead to a dispersion in  $Z_d$ . They include a) grain growth and embryo formation that may deplete micron-size grains and reduce  $\kappa_0$  (D'Alessio et al. 2001), b) extensive orbital evolution of pebbles ( $\sim$  cm-size grains) due to the hydrodynamic drag and turbulent diffusion (Whipple 1972; Supulver & Lin 2000; Ormel & Klahr 2010; Lambrechts & Johansen 2012) to modify and bypass  $M_{\text{iso}}$ , and c) a local concentration of grains and enhancement of  $\Sigma_d$  and  $Z_d$  near the refractory dust and volatile ice condensation/sublimation fronts  $r_{\text{ref}}$  and  $r_{\text{ice}}$  (see §5.2) (Cuzzi & Zahnle 2004; Ciesla & Cuzzi 2006; Chiang & Youdin 2010).

B3) The modest  $\Delta_Z$  assumption is likely to break down with  $Z_d \gg Z_*$  during the advanced evolutionary phase of transitional and debris disks when the residual gas is depleted through viscous accretion and photoevaporation. However, the diminishing  $\dot{M}_a$  (see Eq. 5) is generally too small to enable residual embryos to evolve into cores unless they have already formed at earlier phases. Therefore, in the determination of  $\eta_J$ , we can generally neglect advanced stages of disk evolution.

The aim of our study is to determine the average probability of a supercritical core and an  $\eta_J$ - $Z_*$  correlation. We have already indicated that there is no information on any  $Z_d$  or  $Z_*$  dependence in  $\dot{M}_a$ . All of disks' structural and evolutionary (B1-B3) effects contribute to a dispersion  $\Delta_Z$ . We represent  $\Delta_Z$  to be the logarithm of the disk-metallicity range relative to the stellar metallicity. Here we assume  $\Delta_Z \sim 0.5 - 1$  which corresponds to a factor of 3 – 10 dispersion in metallicity between disks and their central stars. Based on the discussions on the  $Z_d$ - $Z_*$  correlation (A1-A4) and its dispersion (B1-B3), we assume that the amount of heavy elements contained in both the opacity sources (micron-size grains) and building-block planetesimals ( $\Sigma_d$ ) have the following metallicity dispersion:

$$\frac{d^2N}{d\dot{M}_g dZ_d} = A_0 \exp \left[ - \left( \frac{\log(\dot{M}_g/\dot{M}_a)}{\Delta_{\dot{M}_a}} \right)^2 \right] \times \exp \left[ - \left( \frac{(Z_d - Z_*)}{\Delta_Z} \right)^2 \right] \quad (33)$$

which is a more general form of Equation (6).

Analogous to Equation (7), the fraction of stars ( $\eta_Z$ ) that have  $\dot{M}_g$  larger than some fiducial accretion rate  $\dot{M}_f$  with a given set of age, mass  $M_*$ , metallicity  $Z_*$  and  $Z_d$  dispersion is

$$\eta_Z(\dot{M}_f, M_*, Z_*) = \frac{1}{2} \int \text{erfc} \left( \frac{\log[\dot{M}_f(M_*, Z_d)/\dot{M}_a(M_*)]}{\Delta_{\dot{M}_a}} \right) \exp \left[ - \left( \frac{(Z_d - Z_*)}{\Delta_Z} \right)^2 \right] dZ_d. \quad (34)$$

In the above expression, we have taken into account the  $M_*$  dependence but neglected any  $Z_d$  and  $Z_*$  dependence in  $\dot{M}_a$ . The  $\eta_J$ - $Z_*$  correlation can be obtained from  $\eta_Z$

as a function of  $M_*$  and  $Z_*$  by substituting  $\dot{M}_f$  with the critical accretion rate ( $\dot{M}_{\text{res}} = \dot{m}_{g, \text{res}} 10^{-9} M_\odot \text{ yr}^{-1}$ ) for embryos to bypass resonant trapping locations (see §5.4).

## 5.2. Grain condensation, growth, opacity, and viscosity

Equation (30) indicates that the metallicity of the disk gas contributes to  $\dot{m}_{g, \text{res}}$  through both the opacity  $\kappa_0$  and viscosity  $\alpha_\nu$ . We first consider how the disk opacity depends on  $Z_d$ . We adopt the customary assumption that  $\kappa_0 \propto 10^{Z_d}$  but take into account its difference across condensation fronts. In the protostellar disks where very close to the central star, heavy elements are in the gas phase. Refractory grains condense outside the dust destruction front ( $r_{\text{ref}}$ ) where  $T_g \sim 2 \times 10^3$  K, while volatile grains sublimate interior to the snow line ( $r_{\text{ice}}$ ) where  $T_g \sim 170$  K. We parametrize the metallicity and opacity enhancement factors  $\eta_{\text{ice}}$  to be 0, 1, and 4 at  $r < r_{\text{ref}}$ ,  $r_{\text{ref}} < r < r_{\text{ice}}$ , and  $r > r_{\text{ice}}$  respectively.

The midplane temperature in the viscously heated inner disk (GL07) is

$$T_g = 120 m_*^{3/8} \dot{m}_g^{1/2} \alpha_3^{-1/4} \eta_{\text{ice}}^{1/4} \kappa_0^{1/4} r_{\text{AU}}^{-9/8} \text{ K}, \quad (35)$$

so that

$$r_{\text{ref,ice}} = r_\nu m_*^{1/3} \dot{m}_g^{4/9} \alpha_3^{-2/9} \text{ AU} \eta_{\text{ice}}^{2/9} \kappa_0^{2/9} \quad (36)$$

where  $r_\nu = 0.08$ ,  $\eta_{\text{ice}} = 1$  for  $r_{\text{ref}}$  and  $r_\nu = 0.73$ ,  $\eta_{\text{ice}} = 4$  for  $r_{\text{ice}}$  respectively.  $r_{\text{ref}}$  and  $r_{\text{ice}}$  also depend on  $\alpha_\nu$  which might be a function of  $\eta_{\text{ice}}$ . Besides, compared with  $r_{\text{trans}}$  in Eq. (17), the snow line would be within the viscously heated region (i.e.  $r_{\text{ice}} < r_{\text{trans}}$ ) if  $\dot{M}_g$  is greater than

$$\dot{M}_{\text{ice}} = 4.3 \times 10^{-8} m_*^{3/2} \alpha_3^{1/2} \kappa_0^{-1/2} \eta_{\text{ice}}^{-1/2} M_\odot \text{ yr}^{-1}. \quad (37)$$

At  $r > r_{\text{trans}}$ , stellar irradiation leads to

$$T_g = 300 l_*^{2/7} m_*^{-1/7} r_{\text{AU}}^{-3/7} \text{ K}, \quad (38)$$

so that  $r_{\text{ref,ice}} = r_{\text{irr}}$  where  $r_{\text{irr}} = 0.012$  AU,  $\eta_{\text{ice}} = 1$  for  $r_{\text{ref}}$  and  $r_{\text{irr}} = 3.76$  AU,  $\eta_{\text{ice}} = 4$  for  $r_{\text{ice}}$  respectively. For  $\dot{M}_g < \dot{M}_{\text{ice}}$ ,  $r_{\text{trans}} < r_{\text{ice}}$  which can significantly modify the  $T_g$  distribution from those in Equation (35) and (38), and modify the migration rate  $\dot{a}$  in Equation (4) as well (see §5.5).

In addition to condensation/sublimation processes, coagulation/fragmentation processes may also modify the size distribution of grains and the value of  $\kappa_0$ . If these processes lead to an unique equilibrium Mathis, Rumpl, and Nordsieck (MRN, 1977) size ( $s$ ) distribution (as in the interstellar medium), in which  $dN/ds \propto s^{-3.5}$  (Kim et al. 1994), most of the mass would be contained in the large grains, whereas the disk opacity is mainly contributed by grains with size comparable to the wavelength ( $\lambda$ ) of the reprocessed or emitted photons in micron or submillimeter scale. If the MRN size distribution is maintained as grains coagulate into planetesimals and embryos, the magnitude of  $\kappa_0$  would decrease with their growth. Fragmentation, especially collisional cascade, can also replenish small grains.

These uncertainties are taken into account by the dispersion in §5.1 (see Eq. 34). However, a wide (a factor of ten) range of  $\kappa_0$  alone does not significantly modify  $\dot{M}_{g, \text{res}}$  due to its weak dependence on  $\kappa_0$  (Eq. 30). We



now consider how  $Z_d$  may modify the viscosity, *i.e.* the effective magnitude of  $\alpha_3$ .

It is widely assumed that the dominant angular momentum transport mechanism in accretion disks, including protostellar disks, is MHD turbulence. The disk midplane between  $r_{\text{ref}}$  and  $r_{\text{ice}}$  is often thought to be inert because it is cold and neutral (Sano et al. 2000). But the disk surface is partially photoionized by the stellar UV flux. Charged particles recombine on grains and the disk gas establishes an ionization equilibrium. The ionization fraction is an increasing function of distance from the midplane and its value near the disk surface may be adequate to provide an active layer where MHD turbulence can lead to a significant flux of angular momentum transfer (Gammie 1996). The thickness of the active layer is determined by the penetration depth for the stellar X-rays and UV photons (Glassgold et al. 1997) where  $\kappa_{uv}\Delta\Sigma_d \sim 1$ . The column density of dust in the active layer  $\Delta\Sigma_d \propto \kappa_{uv}^{-1} \propto 10^{-Z_d}$ . If the metallicity is constant throughout the disk's vertical structure, the associated fraction of gas in the active layer  $\Delta\Sigma_g \sim 10^{-Z_d}\Delta\Sigma_d \propto 10^{-2Z_d}$ . Thus, the extent of a “dead zone” increases with  $Z_d$ .

Numerical simulations (Turner et al. 2007) indicate the ionization fraction may indeed be suppressed in the dead zone. Nevertheless, MHD waves excited in the active layer continue to induce a modest flux of angular momentum transfer near the mid-plane (Fleming & Stone 2003; Turner & Sano 2008; Kretke & Lin 2012). Reduction of the active layer may also enhance the effect of Ohmic dissipation and ambipolar diffusion which may further suppress MRI in the disk (Bai & Stone 2013). Taking these uncertainties into account, we consider the possibility that the effective  $\alpha_\nu$  may be a decreasing function of  $Z_d$  and explore the implication on the threshold condition for core formation.

In an attempt to construct a quantitative disk-structure model for this effect, we introduced a prescription (Kretke & Lin 2012) in which

$$\alpha_\nu \propto \Delta\Sigma_d \propto \kappa_0^{-1} \propto 10^{-Z_d}. \quad (39)$$

Substituting this prescription into Equation (30) we find  $\dot{M}_{9 \text{ res}} \propto 10^{-Z_d}$ . In this scenario, embryos merge into supercritical cores more readily in disks with higher metallicity due to the threshold condition for orbit crossing rather than the availability of a richer supply of building-block materials.

### 5.3. Simulations of embryo-disk interaction with different $Z_d$ .

We verify the results of above analytic approximation with a series of numerical simulations. For illustrative purposes, we adopt a steady accretion rate ( $\dot{M}_g = 3 \times 10^{-8} M_\odot \text{yr}^{-1}$ ), luminosity  $l_* = 1$  and mass  $m_* = 1$  of a solar-type central star. In the standard model Z1, a set of fiducial opacity ( $\kappa_0 = 1$ ) and viscosity ( $\alpha_3 = 1$ ) is set to those for the solar metallicity ( $Z_d = 0$ ). In model Z2, we set  $\kappa_0 = 3$  and  $\alpha_3 = 1/3$ , which correspond to a metal rich disk with  $Z_d = 0.48$ . In both models Z1 and Z2, we neglect the effect of ice condensation by setting  $\eta_{\text{ice}} = 1$ .

The top two panels of Figure 8 show the type I migration coefficient  $f_a$  in Equation (4). For model Z1,

embryos with  $M_p$  in the range  $\sim 3 - 16 M_\oplus$  migrate outward to  $r_{\text{trans}} = 3.0$  AU. For the more metal-rich model Z2, embryos with  $M_p$  in the range of  $\sim 2 - 13 M_\oplus$  migrate outward to  $r_{\text{trans}} = 6.6$  AU (the red region in the right panel). A comparison between these two models indicates that metallicity enhancement significantly increases with the trapping radius but slightly reduces embryos' optimum trapping mass. This variation is consistent with the analytic approximation  $r_{\text{trans}} \propto \kappa_0^{0.72} \propto 10^{0.72Z_d}$  and  $M_{\text{opt}}(r_{\text{trans}}) \propto \kappa_0^{-0.19} \propto 10^{-0.19Z_d}$  from Equation (28) and (29). Although, with the same  $M_*$  and  $\dot{M}_g$ , the effective temperature distributions in these two models are the same, the midplane temperature in the viscously heated region is elevated in models with enhanced metallicity. This increasing of mid-plane temperature leads to an expansion of the viscously heated region.

With the assumed  $\alpha_\nu - Z_d$  prescription (Eq 39), the viscous dissipation rate actually decreases with  $Z_d$  so that the enhanced metallicity does not significantly modify the aspect ratio ( $H/r$ ) near  $r_{\text{trans}}$ . In Equation (4), the saturation for corotation resonance is at a minimum when  $p_\nu \sim 1$  or  $p_\xi \sim 1$  (Paper II). Minor decreases in  $\nu$  at the new  $r_{\text{trans}}$  also lead to slight decline in  $M_{\text{opt}}(r_{\text{trans}})$ . For these planets,

$$\dot{m}_{9 \text{ res}} \simeq 60 m_*^{0.07} 10^{-Z_d} \quad (40)$$

where we assume  $f_{\text{res}} \simeq 10$  (Papers I and II) in Equation 30.

Six  $5 M_\oplus$  embryos are initially placed within and beyond  $r_{\text{trans}}$  with a separation of  $10 R_R$ . The embryos capture each other into their MMRs in model Z1 (bottom left panel in Fig. 8). This outcome is consistent with our estimate  $\dot{m}_g < \dot{m}_{9 \text{ res}}$ . But embryos are able to marginally cross each other's orbit and undergo cohesive collisions in model Z2 (bottom right panel in Fig. 8).

In addition to the above criterion for bypassing the MMR barrier, the isolation mass  $M_{\text{iso}}$  increases (Eq. 11 & 12), their growth timescale  $\tau_{\text{c,acc}}$  and migration time scale  $\tau_I$  (Eq. 14 & 15) decrease with  $Z_d$ . If, for sufficiently large  $Z_d$ ,  $M_{\text{iso}}$  becomes much larger than  $M_{\text{opt}}$  so that the embryos would migrate into the central stars as their corotation torque becomes saturated. Such a process would deplete  $\Sigma_d$  until  $M_{\text{iso}}$  is reduced to  $\sim M_{\text{opt}}$ .

The upper limit of retainable embryos in models Z1 and Z2 are larger than the critical core mass for the onset of efficient gas accretion  $M_c$ . The enhanced  $Z_d$  also reduces the efficiency of radiation transfer in the envelope around these cores (Ida & Lin 2004a) and increases

$$M_c \simeq 10 \kappa_0^{0.2} M_\oplus = 10^{1+0.2Z_d} M_\oplus \quad (41)$$

as indicated by the white horizontal lines in the upper panels of Figure 8. In model Z2, the merged cores' corotation torque, though weakened, continues to dominate the differential Lindblad torque. These cores migrate outward in the viscously heated inner disk region and are stalled in the proximity of  $r_{\text{trans}}$ . Supercritical cores initially accrete gas on the Kelvin-Helmholtz time scale  $\tau_{\text{KH}} \propto 10^{1.57Z_d}$  (Eq 31). As they initiate efficient and runaway gas accretion, the cores evolve into gas giants *in situ*, perturb the disk structure through gap formation, and undergo type II migration.

### 5.4. The $\eta_J - Z_*$ correlation

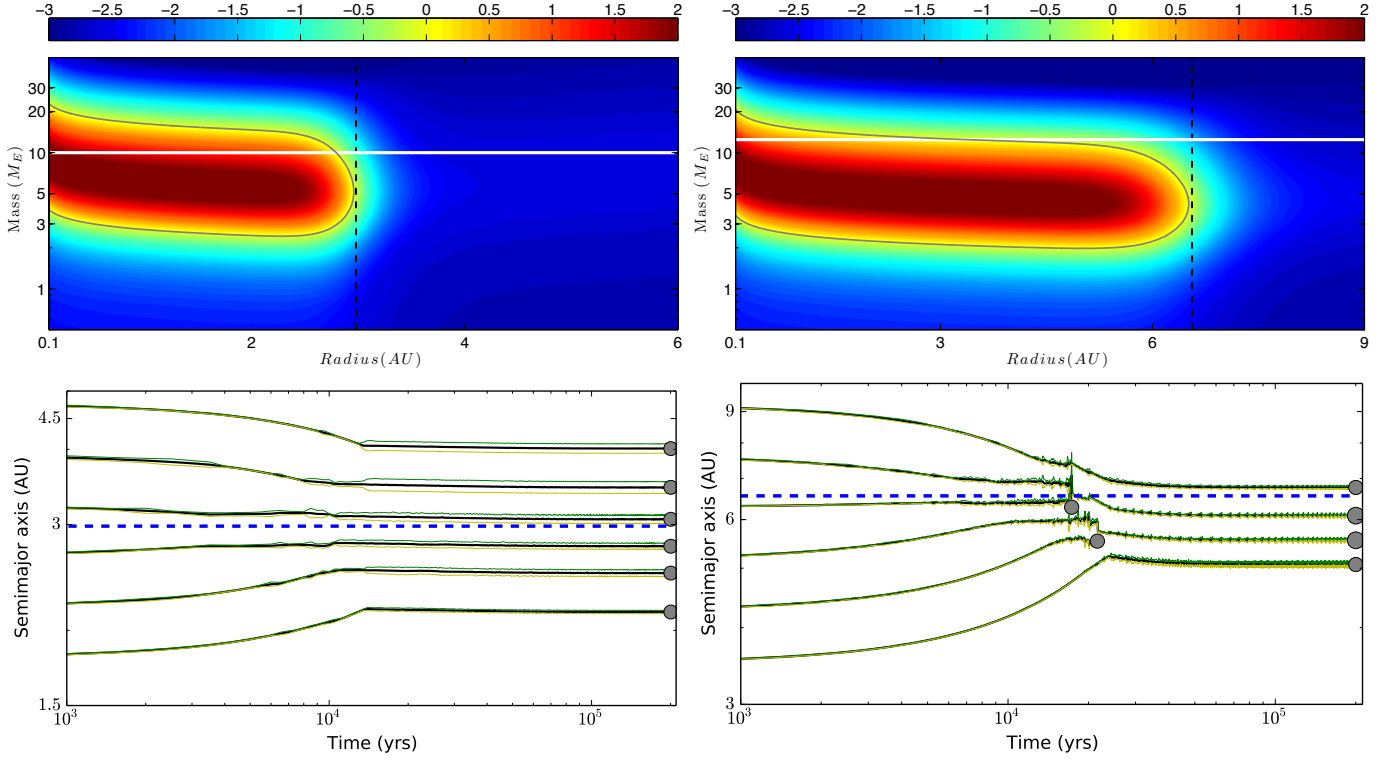


FIG. 8.— **Top:** The type I migration coefficient ( $f_a$ ) for a range of embryos' mass at different locations of the disk. The black dashed line and white line represent the transition radius  $r_{\text{trans}}$  and critical core mass ( $M_c$ ). **Bottom:** orbital evolution of multiple embryos due to their mutual perturbation and tidal interaction with their natal disks. The black lines trace the evolution of embryos' semimajor axis and blue dashed line indicates the location of  $r_{\text{trap}}$ . Green and yellow lines are embryos' apocenter and pericenter distance, respectively. Left and right panels have identical disk parameters ( $\dot{M} = 3 \times 10^{-8} M_\odot/\text{yr}$ ,  $\alpha_\nu = 10^{-3}$  and  $M_* = 1 M_\odot$ ) but slight difference in opacity ( $\kappa_0 = 1$  on the left and  $\kappa_0 = 3$  on the right). Both models contain six  $5 M_\oplus$  embryos, which are initially separated in semimajor axis by  $10 R_R$ , both interior and exterior to the trapping radius.

We construct a  $\eta_J$ - $Z_*$  correlation by substituting  $\dot{M}_{a\odot}$  with  $5 \times 10^{-8} M_\odot \text{yr}^{-1}$  and  $\dot{M}_f$  in Equation (18) with  $\dot{m}_{\text{res}}$  in Equation (40) to obtain

$$\eta_J(M_*, Z_*) = \frac{1}{2} \int \text{erfc} \left( \frac{\log(1.2 m_*^{0.07 - \eta_b} 10^{-Z_d})}{\Delta \dot{M}_a} \right) \exp \left[ - \left( \frac{(Z_d - Z_*)}{\Delta Z} \right)^2 \right] dZ_d. \quad (42)$$

Numerical integration of this equation is shown in Figure 9. Equation (42) indicates that

- 1) the  $\eta_J$ - $M_*$  correlation is primarily due to the average disk accretion rate  $\dot{M}_a$  being an increasing function of the stellar mass  $M_*$ ,
- 2) the  $\eta_J$ - $Z_*$  correlation is primarily due to the critical accretion rate  $\dot{M}_{\text{res}}$  being a decreasing function of the stellar metallicity  $Z_*$ .

The first conclusion is relatively robust and can be verified with future observation. The second conclusion is much more uncertain due to our assumption on the layer accretion scenario and lack of observational constraints on correlation between the stellar and disk metallicity. Nevertheless, these results provide a physical base to account for these correlations.

This theoretical  $\eta_J$ - $M_*$ - $Z_*$  correlation generally agrees with the observations, though the simulated values are somewhat higher than the observed  $\eta_J$  (also noted in

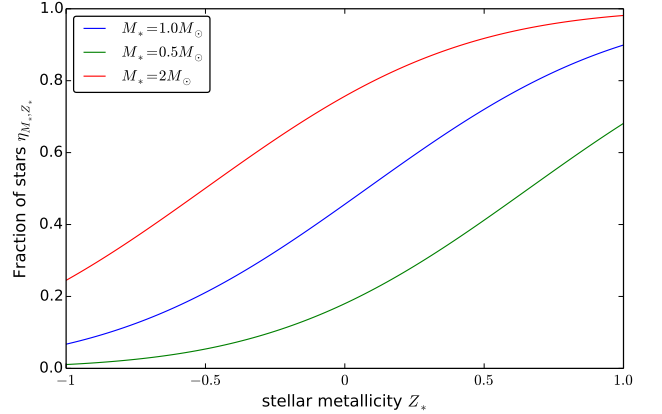


FIG. 9.— The  $\eta_M$  -  $Z_*$  correlation for different stellar masses. The red, green, and blue colors correspond to  $M_* = 2 M_\odot, 1 M_\odot, 0.5 M_\odot$ , respectively.

§4.2). This discrepancy may be attributed in part to (1) the theoretical  $\Sigma_g$ - $\dot{M}_g$  relation derived from the *ad hoc*  $\alpha$  prescription for viscosity, (2) uncertainty in the observationally inferred  $\dot{M}_a$ - $M_*$  correlation, (3) orbital evolution of gas giants, and (4) incompleteness in the observationally determined  $\eta_J$  (Clanton & Gaudi 2014).

### 5.5. Importance of the snow line

For simplicity, we neglected the effect of phase transition due to ice sublimation in the above analysis. In

model Z3, we consider the possibility  $r_{\text{trans}} < r_{\text{ice}}$  in the limit  $\dot{M}_g < \dot{M}_{\text{ice}}$  (see §5.2).

In this case, we set  $\eta_{\text{ice}} = 4$  outside  $r_{\text{ice}}$ . All other parameters of model Z3 are identical to those of model Z1. Figure 10 shows that the distribution of the migration coefficient. The white dashed line represents the snow line  $r_{\text{ice}}$ . Since two different  $\kappa_0$  are adopted (due to the difference in  $\eta_{\text{ice}}$  across the snow line), we find two different trapping locations, which are indicated by black dashed lines. Between these  $r_{\text{trans}}$ , ice condensation/sublimation modifies the  $\Sigma_g$  and  $T_g$  profiles and weakens the corotation torque. Regardless the saturation condition, there is an inward migration region segregated by two trapping radii.

In order to illustrate this effect, we place ten  $3 M_{\oplus}$  embryos across  $r_{\text{ice}}$  in model Z3. Four embryos undergo convergent type I migration to the outer trapping radius, where they bypass their MMR barrier and merge into supercritical cores. The critical core mass  $M_c$  which is  $10 M_{\oplus}$  inside the snow line and  $13 M_{\oplus}$  outside  $r_{\text{ice}}$ .

A merged embryo attained a mass of  $12 M_{\oplus}$ . Since its mass exceeds  $M_{\text{retain}}$ , its corotation torque is saturated and the disk torque on it is dominated by the differential Lindblad torque. It undergoes inward migration until it reaches the inner  $r_{\text{trans}}$  where its orbital evolution is stalled. Along its migration path, it also induced the inward migration of a less massive companion embryo through their mutual MMRs. Two residual  $6 M_{\oplus}$  embryos are left behind near the outer  $r_{\text{trans}}$ . This result highlights the possibility of forming well-separated multiple gas giant systems.

## 6. SUMMARY AND DISCUSSIONS

In this paper, we examine the cause for the  $\eta_{\oplus}$ - $\eta_J$  dichotomy, and the origins of the  $\eta_J$ - $M_*$  and  $\eta_J$ - $Z_*$  correlations.

Following the conventional sequential accretion scenario, we assume that the formation of gas giants is preceded by the emergence of supercritical cores ( $M_c > 10 M_{\oplus}$ ). Based on the omnipresence of super-Earths around stars with a wide range of masses and metallicities, we assume that protoplanetary embryos are common. In addition, multiple-planet systems around low-mass and metal-deficient stars have total mass in excess of the critical value such the rarity of gas giants among these stars is not due to a lack of building-block embryos. We suggest that these embryos undergo extensive convergent migration to a trapping radius likewise at the boundary between the viscously heated inner region and the irradiation heated outer region of the disk. The main deciding factor in their eventual fate is whether their migration is sufficiently fast to enable them to overcome their mutual resonant barrier.

Using a set of steady-state disk models for protoplanetary disks around classical T Tauri stars, we determine the critical surface density distribution for the disk gas that would induce adequate torque for embryos to undergo orbit crossing, close encounters and collisional coalescence. Since it is difficult to measure the surface density of both gas and dust in protostellar disks, we translate the critical condition into critical gas accretion rate ( $\dot{M}_{\text{res}}$ ). With an *ad hoc*  $\alpha$  layer structure model, we carry out analytic treatment and some numerical simulations

to show that  $\dot{M}_{\text{res}}$  weakly depends on  $M_*$  and decreases with  $Z_d$ . Based on observational data on protostellar disks, we infer that the actual accretion rate increases with the stellar mass and is independent of the stellar metallicity. When applied to our models, we find that embryos are more likely to merge into supercritical cores around relatively massive and metal-rich stars.

Our results provide the necessary condition for the formation of gas giants. We link this threshold condition to the cause of  $\eta_J$ - $M_*$  and  $\eta_J$ - $Z_*$  correlations. In the forthcoming papers of this series, we determine how the rapid growth of gas giants may affect the disk structure and perturb the orbits of nearby embryos. We also need to take into account gas giants' type II migration and to generalize these models to evolving (rather than steady) disks. During the advanced stage of their natal disks' evolution, both the super-Earths and gas giants may evolve into their asymptotic (present-day) orbital configuration as the trapping radius contracts with the depletion of the gas. Finally, we will incorporate the results of these investigations into our population synthesis models (Ida et al. 2013) and simulate the observed  $M_p$ - $a_p$  distribution for stars with different  $M_*$  and  $Z_*$ .

The authors thank S. Aarseth, C. Baruteau, S. Ida, K. Kretke, H. Li, T. Kouwenhoven, K. Schlaufman, A. Wolfgang, Y. Huang, S. Dong, C. Ormel and C. Dominik for useful conversations and an anonymous referee for helpful comments. This work is supported by an UC/Lab grant and an IGPPS grant. B.Liu also thanks T. Kouwenhoven for support by an NSFC grant.

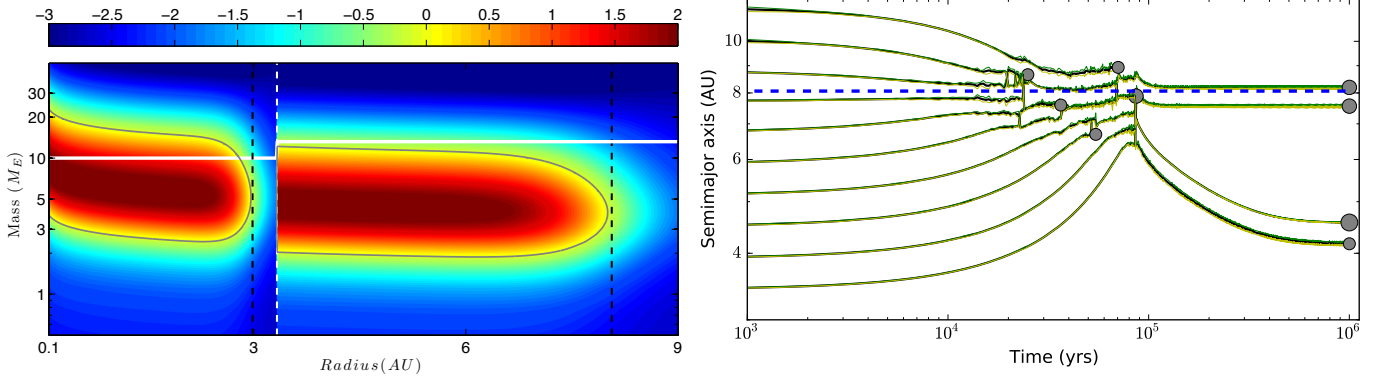


FIG. 10.— **Left:** The type I migration coefficient ( $f_a$ ) for a range of embryos' masses at different locations in the disk. The two black dashed lines represent the transition radii  $r_{\text{trans}}$  associated with silicate and ice grain opacities. The white dashed line represents the snow line. The white solid line represents the critical core mass for the onset of efficient gas accretion. **Right:** The mutual interaction between embryos and their natal disks in model Z3. The black lines trace the evolution of embryos' semi-major axis and blue dashed line indicates the location of  $r_{\text{trap}}$ . Green and yellow lines are embryos' apocenter and pericenter distance, respectively. Disk parameters are chosen  $\dot{M} = 3 \times 10^{-8} M_{\odot}/\text{yr}$ ,  $\alpha_{\nu} = 10^{-3}$ ,  $M_* = 1 M_{\odot}$ ,  $\kappa_0 = 1$ , and  $\eta_{\text{ice}} = (1, 4)$  inside or outside the snow line. Model Z3 contains ten  $3 M_{\oplus}$  embryos which are initially distributed on either side of the trapping radius with  $10 R_R$  separation.

## APPENDIX

TABLE 2  
LIST OF NOTATIONS

Variables	Meaning	Definition
$M_c$	Critical core mass for initiating rapid gas accretion onto the core	
$M_{\text{opt}}$	Optimum embryo mass for unsaturated corotation torque and outward migration in viscous region	eq. (16)
$M_{\text{retain}}$	Upper limit embryo mass for unsaturated corotation torque and outward migration in viscous region	
$M_{\text{iso}<}$	Isolation mass of the planet for inner viscous region	eq. (11)
$M_{\text{iso}>}$	Planet isolation mass of the planet for outer irradiated region	eq. (12)
$M_p$	Single planet mass	
$M_s$	Total planet mass in individual planetary system	
$M_*$	Stellar mass	
$Z_*$	Stellar metallicity	
$\dot{M}_g$ or $\dot{M}_d$	Gas accretion rate	
$\dot{M}_a$	Average gas accretion rate	eq. (5)
$\dot{M}_f$	Threshold gas accretion rate that embryos merge into retainable cores	eq. (8)
$\dot{M}_{\text{cr}}$	Normalized factor of $\dot{M}_f$	eq. (8)
$\dot{M}_{\text{ice}}$	Threshold gas accretion rate when $r_{\text{trans}} = r_{\text{ice}}$	eq. (37)
$\dot{M}_{\text{res}}$	Critical gas accretion rate for breaking mean motion resonance	eq. (8)
$\dot{m}_{g \text{ res}}$	$\dot{M}_{\text{res}}/10^{-9} M_{\odot}\text{yr}^{-1}$	eq. (18)
$R_R$	Roche radius of the planet	
$R_p$	Physical radius of the planet	
$k_0$	Final mean separation in unit of Roche radius	
$f_a$	Type I migration coefficient	eq. (4)
$\Gamma$	Total net disk torque for a planet	eq. (3)
$\eta_{\dot{M}(\dot{M}_f, M_*, Z_*)}$	Fraction of stars with $M_*$ and $Z_*$ has $\dot{M}_g$ larger than fiducial value $\dot{M}_f$	eq. (7)
$\eta_a$	Fitting power-law index for gas accretion rate and age relationship	eq. (5)
$\eta_b$	Fitting power-law index for gas accretion rate and stellar mass relationship	eq. (5)
$\eta_c$	Fitting power-law index for $\dot{M}_f$ and stellar mass relationship	eq. (8)
$\eta_J$	Fraction of stars containing gas giant planets	
$\eta_{\oplus}$	Fraction of stars containing super Earth planets	
$\tau_{c, \text{acc}}$	Gas accretion time scale when the core reaches critical mass	eq. (10)
$\tau_{\text{dep}}$	Depletion time scale of disk gas	
$\tau_{\text{KH}}$	Kelvin-Helmholtz contraction time scale of gas envelope	eq. (24)
$\tau_{\text{I}}$	Type I migration time scale of a planet	eq. (13)
$\tau_{\text{I}<}$	Type I migration time scale of a planet in inner viscous region	eq. (14)
$\tau_{\text{I}>}$	Type I migration time scale of a planet in outer irradiated region	eq. (15)
$\Sigma_d$	Dust surface density of a disk	
$\Sigma_g$	Gas surface density of a disk	
$T_g$	Disk gas temperature	
$\eta_{\text{ice}}$	An enhancement factor of $\Sigma_d$ due to ice condensation	
$r_{\text{trans}}$	Trapping or transition radius separates the inner viscous and outer irradiated disk region	eq. (17)
$r_{\text{ref, ice}}$	Radius for dust destruction or ice condensation	eq. (36)

## REFERENCES

- Anders, E., & Grevesse, N. 1989, *Geochim. Cosmochim. Acta*, 53, 197
- Andrews, S. M., Rosenfeld, K. A., Kraus, A. L., & Wilner, D. J. 2013, *ApJ*, 771, 129
- Bai, X.-N., & Stone, J. M. 2013, *ApJ*, 769, 76
- Baillie, K., Charnoz, S., & Pantin, E. 2015, *A&A*, 577, A65
- Baruteau, C., Cuadra, J., & Lin, D. N. C. 2011, *ApJ*, 726, 28
- Baruteau, C., et al. 2014, *Protostars and Planets VI*, 667
- Beckwith, S. V. W., Sargent, A. I., Chini, R. S., & Guesten, R. 1990, *AJ*, 99, 924
- Bitsch, B., Crida, A., Morbidelli, A., Kley, W., & Dobbs-Dixon, I. 2013, *A&A*, 549, A124
- Bitsch, B., & Kley, W. 2010, *A&A*, 523, A30
- Bonfils, X., et al. 2013, *A&A*, 549, A109
- Buchhave, L. A., et al. 2012, *Nature*, 486, 375
- . 2014, *Nature*, 509, 593
- Chatterjee, S., & Tan, J. C. 2014, *ApJ*, 780, 53
- Chiang, E., & Youdin, A. N. 2010, *Annual Review of Earth and Planetary Sciences*, 38, 493
- Ciesla, F. J., & Cuzzi, J. N. 2006, *Icarus*, 181, 178
- Clanton, C., & Gaudi, B. S. 2014, *ApJ*, 791, 91
- Coleman, G. A. L., & Nelson, R. P. 2014, *MNRAS*, 445, 479
- Cossou, C., Raymond, S. N., Hersant, F., & Pierens, A. 2014, *A&A*, 569, A56
- Cumming, A., Butler, R. P., Marcy, G. W., Vogt, S. S., Wright, J. T., & Fischer, D. A. 2008, *PASP*, 120, 531
- Cuzzi, J. N., & Zahnle, K. J. 2004, *ApJ*, 614, 490
- Da Rio, N., Jeffries, R. D., Manara, C. F., & Robberto, M. 2014, *MNRAS*, 439, 3308
- D'Alessio, P., Calvet, N., & Hartmann, L. 2001, *ApJ*, 553, 321
- D'Antona, F., & Mazzitelli, I. 1994, *ApJS*, 90, 467
- Dong, S., & Zhu, Z. 2013, *ApJ*, 778, 53
- Dressing, C. D., & Charbonneau, D. 2013, *ApJ*, 767, 95
- Dressing, C. D., et al. 2015, *ApJ*, 800, 135
- Endl, M., Cochran, W. D., Kürster, M., Paulson, D. B., Wittenmyer, R. A., MacQueen, P. J., & Tull, R. G. 2006, *ApJ*, 649, 436
- Ercoleano, B., Mayr, D., Owen, J. E., Rosotti, G., & Manara, C. F. 2014, *MNRAS*, 439, 256
- Fischer, D. A., & Valenti, J. 2005, *ApJ*, 622, 1102
- Fleming, T., & Stone, J. M. 2003, *ApJ*, 585, 908
- Fressin, F., et al. 2013, *ApJ*, 766, 81
- Gammie, C. F. 1996, *ApJ*, 457, 355
- Garaud, P., & Lin, D. N. C. 2007, *ApJ*, 654, 606
- Garcia Lopez, R., Natta, A., Testi, L., & Habart, E. 2006, *A&A*, 459, 837
- Glassgold, A. E., Najita, J., & Igea, J. 1997, *ApJ*, 480, 344
- Goldreich, P., & Tremaine, S. 1980, *ApJ*, 241, 425
- Hartmann, L. 1998, *Accretion Processes in Star Formation*
- Hartmann, L., Calvet, N., Gullbring, E., & D'Alessio, P. 1998, *ApJ*, 495, 385
- Hasegawa, Y., & Pudritz, R. E. 2010, *ApJ*, 710, L167
- Hayashi, C. 1981, *Progress of Theoretical Physics Supplement*, 70, 35
- Howard, A. W., et al. 2012, *ApJS*, 201, 15
- Huber, D., et al. 2014, *ApJS*, 211, 2
- Hubickyj, O., Bodenheimer, P., & Lissauer, J. J. 2005, *Icarus*, 179, 415
- Ida, S., & Lin, D. N. C. 2004a, *ApJ*, 604, 388
- . 2004b, *ApJ*, 616, 567
- . 2005, *ApJ*, 626, 1045
- . 2008, *ApJ*, 673, 487
- Ida, S., Lin, D. N. C., & Nagasawa, M. 2013, *ApJ*, 775, 42
- Ikoma, M., Nakazawa, K., & Emori, H. 2000, *ApJ*, 537, 1013
- Johnson, J. A., Aller, K. M., Howard, A. W., & Crepp, J. R. 2010, *PASP*, 122, 905
- Johnson, J. A., Butler, R. P., Marcy, G. W., Fischer, D. A., Vogt, S. S., Wright, J. T., & Peek, K. M. G. 2007, *ApJ*, 670, 833
- Jones, M. I., et al. 2016, *ArXiv e-prints*
- Kim, S.-H., Martin, P. G., & Hendry, P. D. 1994, *ApJ*, 422, 164
- Kley, W., & Nelson, R. P. 2012, *ARA&A*, 50, 211
- Kretke, K. A., & Lin, D. N. C. 2007, *ApJ*, 664, L55
- . 2012, *ApJ*, 755, 74
- Lambrechts, M., & Johansen, A. 2012, *A&A*, 544, A32
- Laughlin, G., Bodenheimer, P., & Adams, F. C. 2004a, *ApJ*, 612, L73
- Laughlin, G., Steinacker, A., & Adams, F. C. 2004b, *ApJ*, 608, 489
- Lee, M. H., & Peale, S. J. 2002, *ApJ*, 567, 596
- Li, R., Lin, D., Zhang, Y., & Dong, B. 2016, *ApJ* in prep.
- Lin, D. N. C., Bodenheimer, P., & Richardson, D. C. 1996, *Nature*, 380, 606
- Lin, D. N. C., & Papaloizou, J. 1986, *ApJ*, 309, 846
- Lin, D. N. C., & Papaloizou, J. C. B. 1993, in *Protostars and Planets III*, ed. E. H. Levy & J. I. Lunine, 749–835
- Lissauer, J. J., et al. 2011, *ApJS*, 197, 8
- Liu, B., Zhang, X., Lin, D. N. C., & Aarseth, S. J. 2015, *ApJ*, 798, 62
- Lopez, E. D., & Fortney, J. J. 2014, *ApJ*, 792, 1
- Lyra, W., Paardekooper, S.-J., & Mac Low, M.-M. 2010, *ApJ*, 715, L68
- Manara, C. F., Robberto, M., Da Rio, N., Lodato, G., Hillenbrand, L. A., Stassun, K. G., & Soderblom, D. R. 2012, *ApJ*, 755, 154
- Marcy, G. W., et al. 2008, *Physica Scripta Volume T*, 130, 014001
- . 2014, *ApJS*, 210, 20
- Masset, F. S., Morbidelli, A., Crida, A., & Ferreira, J. 2006, *ApJ*, 642, 478
- Mordasini, C., Alibert, Y., Benz, W., Klahr, H., & Henning, T. 2012, *A&A*, 541, A97
- Mortier, A., Santos, N. C., Sousa, S. G., Adibekyan, V. Z., Delgado Mena, E., Tsantaki, M., Israelian, G., & Mayor, M. 2013, *A&A*, 557, A70
- Movshovitz, N., Bodenheimer, P., Podolak, M., & Lissauer, J. J. 2010, *Icarus*, 209, 616
- Mulders, G. D., Pascucci, I., & Apai, D. 2015, *ApJ*, 798, 112
- Murray, C. D., & Dermott, S. F. 1999, *Solar system dynamics*
- Natta, A., Testi, L., & Randich, S. 2006, *A&A*, 452, 245
- Nelson, R. P. 2005, *A&A*, 443, 1067
- Ogihara, M., & Kobayashi, H. 2013, *ApJ*, 775, 34
- Ormel, C. W., & Klahr, H. H. 2010, *A&A*, 520, A43
- Ormel, C. W., & Kobayashi, H. 2012, *ApJ*, 747, 115
- Paardekooper, S.-J., Baruteau, C., Crida, A., & Kley, W. 2010, *MNRAS*, 401, 1950
- Paardekooper, S.-J., Baruteau, C., & Kley, W. 2011, *MNRAS*, 410, 293
- Papaloizou, J. C. B., & Szuszkiewicz, E. 2005, *MNRAS*, 363, 153
- Pierens, A., Cossou, C., & Raymond, S. N. 2013, *A&A*, 558, A105
- Pierens, A., & Nelson, R. P. 2008, *A&A*, 482, 333
- Pollack, J. B., Hubickyj, O., Bodenheimer, P., Lissauer, J. J., Podolak, M., & Greenzweig, Y. 1996, *Icarus*, 124, 62
- Ramírez, I., Meléndez, J., Cornejo, D., Roederer, I. U., & Fish, J. R. 2011, *ApJ*, 740, 76
- Ramírez, I., et al. 2015, *ApJ*, 808, 13
- Rogers, L. A. 2015, *ApJ*, 801, 41
- Ros, K., & Johansen, A. 2013, *A&A*, 552, A137
- Ruden, S. P., & Lin, D. N. C. 1986, *ApJ*, 308, 883
- Sano, T., Miyama, S. M., Umebayashi, T., & Nakano, T. 2000, *ApJ*, 543, 486
- Santos, N. C., Israelian, G., & Mayor, M. 2004, *A&A*, 415, 1153
- Schlaufman, K. C. 2015, *ApJ*, 799, L26
- Schlaufman, K. C., & Laughlin, G. 2011, *ApJ*, 738, 177
- Shakura, N. I., & Sunyaev, R. A. 1973, *A&A*, 24, 337
- Shen, Z.-X., Jones, B., Lin, D. N. C., Liu, X.-W., & Li, S.-L. 2005, *ApJ*, 635, 608
- Sousa, S. G., Santos, N. C., Israelian, G., Mayor, M., & Udry, S. 2011, *A&A*, 533, A141
- Sousa, S. G., et al. 2008, *A&A*, 487, 373
- Supulver, K. D., & Lin, D. N. C. 2000, *Icarus*, 146, 525
- Tanaka, H., Takeuchi, T., & Ward, W. R. 2002, *ApJ*, 565, 1257
- Terquem, C. E. J. M. L. J. 2003, *MNRAS*, 341, 1157
- Turner, N. J., & Sano, T. 2008, *ApJ*, 679, L131
- Turner, N. J., Sano, T., & Dziourkevitch, N. 2007, *ApJ*, 659, 729
- Wang, J., & Fischer, D. A. 2015, *AJ*, 149, 14
- Ward, W. R. 1997, *Icarus*, 126, 261
- Weiss, L. M., & Marcy, G. W. 2014, *ApJ*, 783, L6
- Whipple, F. L. 1972, in *From Plasma to Planet*, ed. A. Elvius, 211
- Wilden, B. S., Jones, B. F., Lin, D. N. C., & Soderblom, D. R. 2002, *AJ*, 124, 2799
- Winn, J. N., & Fabrycky, D. C. 2015, *ARA&A*, 53, 409
- Wolfgang, A., Rogers, L. A., & Ford, E. B. 2015, *ArXiv e-prints*
- Wu, Y., & Lithwick, Y. 2013, *ApJ*, 772, 74
- Zeng, L., & Sasselov, D. 2013, *PASP*, 125, 227
- Zeng, L., Sasselov, D. D., & Jacobsen, S. B. 2016, *ApJ*, 819, 127
- Zhang, X., Liu, B., Lin, D. N. C., & Li, H. 2014, *ApJ*, 797, 20
- Zhou, J.-L., Lin, D. N. C., & Sun, Y.-S. 2007, *ApJ*, 666, 423